Implementation of a GPU-enhanced multiclass soil erosion model based on the 2D shallow water equations in the software Iber

Luis Cea, Orlando García-Feal, Guillaume Nord, Guillaume Piton, Cédric Legoût

Environmental Modelling and Software 179 (2024) 106098

Contents lists available at ScienceDirect

Environmental Modelling and Software

journal homepage: www.elsevier.com/locate/envsoft

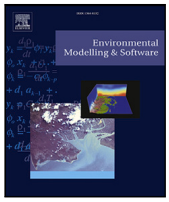

Position Paper

Implementation of a GPU-enhanced multiclass soil erosion model based on the 2D shallow water equations in the software Iber

Luis Cea [a,*], Orlando García-Feal [a,b], Guillaume Nord [c], Guillaume Piton [c], Cédric Legoût [c]

[a] Universidade da Coruña, Water and Environmental Engineering Group, Center for Technological Innovation in Construction and Civil Engineering (CITEEC), Campus de Elviña, s/n, A Coruña, 15071, Spain
[b] Centro de Investigación Mariña, Universidade de Vigo, Environmental Physics Laboratory (CIM-EPhysLab), Campus Auga, Ourense, 32004, Spain
[c] Univ. Grenoble Alpes, INRAE, CNRS, IRD, Grenoble INP, IGE, Grenoble, 38000, France

ARTICLE INFO

Dataset link: https://entrepot.recherche.data.gouv.fr/dataverse/soilsedimentmodellingdata

Keywords:
Soil erosion
Sediment transport
Distributed numerical modelling
Shallow water equations
High performance computing

ABSTRACT

We present the implementation of a new fully distributed multiclass soil erosion module. The model is based on a 2D finite volume solver (Iber+) for the 2D shallow water equations that computes the overland flow water depths and velocities. From these, the model evaluates the transport of sediment particles due to bed load and suspended load, including rainfall-driven and runoff-driven erosion processes, and using well-established physically-based formulations. The evolution of the mass of sediment particles in the soil layer is computed from a mass conservation equation for each sediment class. The solver is implemented using High Performance Computing techniques that take advantage of the computational capabilities of standard Graphical Processing Units, achieving speed-ups of two orders of magnitude relative to a sequential implementation on the CPU. We show the application and validation of the model at different spatial scales, ranging from laboratory experiments to meso-scale catchments.

1. Introduction

Soil erosion and sediment transport involve complex processes at different spatial and temporal scales, including the detachment of soil particles, the transport and redistribution of these particles by the overland flow, and eventually their deposition in regions different from where they were eroded. All these processes can have important impacts on the environment and economy making it necessary to implement soil management practices (Pimentel et al., 1995). A correct understanding of the role of these processes at the basin and river reach scales is needed for an efficient management of soil erosion-related problems as soil loss, muddy floods, freshwater pollution or reservoir siltation, among others.

Soil erosion models are tools that can be useful to help decision-making in soil management, however they must be rigorously evaluated, properly calibrated and considering the inherent uncertainties present in models and observed data (Batista et al., 2019). The soil erosion models at a catchment scale can be classified following the spatial discretisation method used (Arnold et al., 2010; Fu et al., 2019): lumped models where the whole catchment have a fixed set of parameters like EPIC (Williams et al., 1984) and other Universal Soil Loss Equation (USLE) based models (Pandey et al., 2016); semi-distributed models with discretisation in spatial units based on land properties considering flow routing between the units or not like WEPP (Flanagan et al., 2012), EUROSEM (Morgan et al., 1998) or SWAT (Arnold et al., 1998); and distributed models where the catchment is divided into a computational grid or mesh in which each element has its own properties and connected to their neighbours like SWATgrid (Arnold et al., 2010) or WRF-Hydro-Sed (Yin et al., 2020).

Physically-based distributed soil erosion models can contribute to the understanding and interpretation of laboratory and *in-situ* measurements and therefore, to the analysis of the processes involved in soil erosion (Fu et al., 2019). However, distributed models typically require a high amount of input data and their computational cost is much higher than lumped or semi-distributed models, limiting their application to small watersheds (Pignotti et al., 2017). Once calibrated and validated with experimental or field data, a numerical model can be used to complement the available observations, and to validate or propose new hypothesis.

Several recent studies have shown that, with a proper calibration of bed friction and infiltration, and a well-defined Digital Terrain Model (DTM), the 2D Shallow Water Equations (2D-SWE) are able to correctly reproduce water depths, velocities, and discharges under surface runoff conditions (Cea et al., 2014; Mügler et al., 2011; Tatard et al., 2008), and are therefore a good basis for physically-based soil erosion models.

* Corresponding author.
E-mail addresses: luis.cea@udc.es (L. Cea), orlando@uvigo.es (O. García-Feal).

https://doi.org/10.1016/j.envsoft.2024.106098
Received 1 September 2023; Received in revised form 9 May 2024; Accepted 6 June 2024
Available online 8 June 2024

At the same time, several physically-based formulations that represent these processes at their lowest scales have been proposed and tested in laboratory and field experiments (Beuselinck et al., 1999, 2002; Foster et al., 1995; Govers, 1992; Hairsine and Rose, 1992a,b; Jomaa et al., 2010; Kinnell, 1990, 2005; Nord and Esteves, 2007; Shaw et al., 2006, 2009), and have been shown to be a good basis to be implemented in a distributed erosion model (Cea et al., 2016; Heng et al., 2011; Nord and Esteves, 2005, 2007; Tromp-van Meerveld et al., 2008; Ouyang et al., 2023). In order to take advantage of their full potential these formulations require a detailed definition of the sediment properties, as well as an accurate spatial characterisation of the flow field, and therefore of the topography, land use, rainfall intensity and infiltration.

In addition to these erosion models, which were developed to represent soil erosion processes from the plot to the small catchment, there are hydrodynamic and morphodynamic models, which were initially developed to represent erosion and sediment transport processes (suspension and transport) in the fluvial or even coastal environment. Amongst these models, we can cite the initial version of Iber (Bladé et al., 2014), iRIC (Shimizu et al., 2020), BASEMENT (Vanzo et al., 2021) and GAIA (Tassi et al., 2023). There is currently an interest in bridging the gap between these hillslope and fluvial models and taking hydrological processes into account in order to understand the spatio-temporal dynamics of sediment transfers in the headwaters and medium scale catchments (< 100 km^2), involving diffuse sources of erosion on hillslopes (erosion by rainfall or overland flow), local sources of erosion in the hydrographic network (river bed, river bank, landslide), transport and deposition processes. Some modelling attempts in this way can be cited (Coulthard and Skinner, 2016; Taccone et al., 2018; Batista et al., 2019). To study the connection between hillslopes and rivers, which lies at the interface between different scientific communities (hydrology, soil science, hydraulics, geomorphology), it is necessary to develop new tools with high spatial and temporal resolution.

This paper presents an event-scale two-dimensional soil erosion and sediment transport model that can be applied from the plot or reach scale to the catchment scale. The model is implemented in the software Iber (Bladé et al., 2014), which computes the overland flow velocities and water depths from the 2D-SWE, including rainfall and infiltration terms over the whole domain indistinctly, so that there is total continuity between the hillslopes and the river. Soil erosion by rainfall and overland flow is computed using physically-based formulations, considering multiple sediment classes that might be transported either as suspended load or as bed load. A 2D transport equation is solved for each sediment class, considering convective transport and deposition of sediment particles. Changes in the topography are computed from the 2D Exner equation, and considered in the hydrodynamic equations in order to couple the sediment transport with the overland flow. The hydrodynamic equations, as well as the sediment transport and Exner equations are solved with a GPU-enhanced finite volume solver, taking advantage of High Performance Computing (HPC) techniques and achieving speed-ups up to two orders of magnitude respect to the non parallelised version. This is essential in order to solve the equations with a high spatial and temporal resolution, while keeping computational times relatively low, addressing one of the main limitations of fully-distributed models. Thus, this article introduces a tool that makes it possible to compute and analyse erosion and sediment transport processes at multiple locations and scales as plots on hillslopes, river reaches and catchments, by solving physically-based equations with a temporal and spatial resolution much higher than standard soil erosion models by implementing GPU-computing acceleration, being a relatively unexplored solution for this specific field. The tool presented in this article has the advantage of being a freely-available product. It is distributed on an up-to-date platform (https://www.iberaula.es/). Training courses are offered to users on a regular basis. The model is versatile and can be used for a wide range of research, teaching and engineering applications.

The paper is organised as follows. Section 2 describes the soil erosion processes included in the model and their mathematical representation. Section 3 presents the numerical schemes used to solve the model equations, as well as the High Performance Computing implementation that makes use of the computational capabilities of Graphical Processing Units (GPU). Section 4 presents four test cases that cover different potential applications of the model, including the calibration and validation of the model with observed data at the laboratory scale and at the field scale. Section 5 summarises the main conclusions, capabilities and limitations of the model.

2. Model equations

This section presents the mathematical equations solved by the soil erosion model. The overland flow equations are presented briefly, since they are well-known and have already been discussed and validated for river and surface runoff applications in many previous studies. The soil erosion equations are presented in more detail, since their implementation differs from other soil erosion models, specially at the hillslope and catchment scales.

2.1. Hydrodynamic equations

The overland flow water depths and velocities are computed from the hydrodynamic module of the software Iber, which solves the 2D-SWE including rainfall and infiltration terms (Bladé et al., 2014; Cea and Bladé, 2015):

$$\frac{\partial h}{\partial t} + \frac{\partial q_x}{\partial x} + \frac{\partial q_y}{\partial y} = r - f \tag{1}$$

$$\frac{\partial q_x}{\partial t} + \frac{\partial}{\partial x}\left(\frac{q_x^2}{h} + \frac{g h^2}{2}\right) + \frac{\partial}{\partial y}\left(\frac{q_x q_y}{h}\right) = -g h \frac{\partial z_b}{\partial x} - g h I_x \tag{2}$$

$$\frac{\partial q_y}{\partial t} + \frac{\partial}{\partial x}\left(\frac{q_x q_y}{h}\right) + \frac{\partial}{\partial y}\left(\frac{q_y^2}{h} + \frac{g h^2}{2}\right) = -g h \frac{\partial z_b}{\partial y} - g h I_y \tag{3}$$

where x and y are the two horizontal directions, t is the time, z_b is the bed elevation, h is the water depth, (q_x, q_y) are the two components of the unit discharge in the two horizontal directions, (I_x, I_y) are the two components of the bed friction slope, g is the gravity acceleration, r is the rainfall rate and f is the infiltration rate. The two components of the depth averaged water velocity (U_x, U_y) are computed as the ratio between the corresponding unit discharges and the water depth. The bed friction slope can be computed using any empirical formulation, such as those of Manning, Chezy or Keulegan. In all the case studies presented in this work the formulation of Manning was used.

2.2. Soil erosion conceptual model

The soil erosion model considers that the sediment is formed by a mixture of N_p particle classes with a different characteristic diameter (D_k, with $k = 1, N_p$). The vertical structure of the soil is represented as a layer of loose sediment (low cohesion) lying over a layer of the original soil matrix (Fig. 1). Below the original soil layer lies a non-erodible rock layer that limits the maximum soil erosion. The mass fraction of each particle class in the loose sediment and original soil layers might be different and is represented by f_k and g_k respectively in Fig. 1. The size distribution of sediment in the original soil layer (g_k) is defined by the user as input data, with the only restriction that the sum of the mass fractions for all classes must be equal to 1 (i.e., $\sum g_k = 1$). On the other hand, the spatial and temporal evolution of the mass fractions in the loose sediment layer (f_k) is computed by the model, ensuring also that the sum over all fractions is equal to one ($\sum f_k = 1$). The initial mass of each particle class in the loose sediment layer must also be defined by the user as an initial condition, and might vary in space.

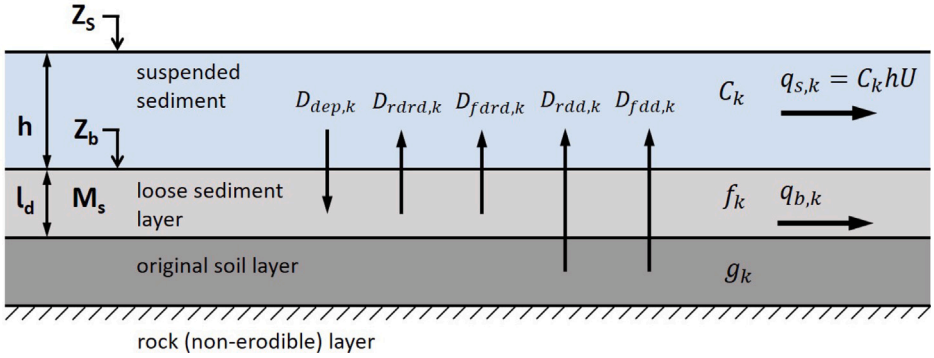

Fig. 1. Vertical structure of the soil and components of the soil erosion model.

The total mass of sediment per unit surface in the loose sediment layer (M_s) and its thickness (l_d) are related by:

$$l_d = \frac{M_s}{\rho_s \phi} \tag{4}$$

where ρ_s is the mass density of the solid particles and ϕ is the porosity of the soil layer. From Eq. (4), an equivalent thickness for each sediment fraction ($l_{d,k}$) in the loose sediment layer can be defined as (assuming that all sediment classes have the same mass density):

$$l_{d,k} = \frac{l_d}{M_s} M_{s,k} = \frac{M_{s,k}}{\rho_s \phi} \tag{5}$$

where $M_{s,k}$ is the mass per unit surface of sediment class k in the loose sediment layer.

Two modes of transport are considered for each sediment class: bed load and suspended load ($q_{b,k}$ and $q_{s,k}$ respectively in Fig. 1). Suspended load takes place over the whole water column, assuming that the sediment particles move with the depth-averaged water velocity (same modulus and direction). The depth-averaged suspended sediment concentration for each class (C_k) is computed from a mass conservation equation that considers the detachment of sediment from both the loose sediment and the original soil layers, as well as the deposition of sediment in the eroded layer, as it will be detailed in the following section.

Bed load takes place in the upper part of the loose sediment layer and therefore, it is subject to the availability of sediment in that layer. The movement of particles that are transported as bed load is computed using a standard empirical bed load formulation, as detailed in Section 2.4.

All the mathematical equations used to represent these processes are described in the following subsections.

2.3. Suspended load

Suspended load for sediment class k is computed as $q_{s,k} = C_k |U| h$, where $|U|$ is the modulus of the depth-averaged velocity and C_k is the depth-averaged suspended sediment concentration of class k. The temporal and spatial evolution of the concentration for each sediment class is computed from the following depth-averaged scalar transport equation:

$$\frac{\partial h C_k}{\partial t} + \frac{\partial q_x C_k}{\partial x} + \frac{\partial q_y C_k}{\partial y} = D_{rdd,k} + D_{rdrd,k} + D_{fdd,k} + D_{fdrd,k} + D_{dep,k} \tag{6}$$

where $D_{rdd,k}$ and $D_{fdd,k}$ are the rainfall-driven and flow-driven detachment rates of sediment class k from the original soil layer, $D_{rdrd,k}$ and $D_{fdrd,k}$ are the rainfall-driven and flow-driven redetachment rates of sediment class k from the loose sediment layer, and $D_{dep,k}$ is the deposition rate of sediment class k from the water column into the loose sediment layer (Fig. 1). All the source terms in Eq. (6) are expressed in $kg/m^2/s$. The model can also consider horizontal mass transfer due to turbulent diffusion, but the related terms were omitted in Eq. (6) for the sake of conciseness, since in the applications presented in this work its influence is negligible compared to the other terms in the equation.

If the rainfall and flow driven redetachment rates are larger than the deposition rate (i.e. $D_{rdrd,k} + D_{fdrd,k} > D_{dep,k}$), there is a net transfer of sediment particles of class k from the loose sediment layer to the water column. Conversely, if deposition exceeds the sum of both redetachment rates, the mass of sediment class k in the loose sediment layer will increase.

The rainfall driven detachment and redetachment rates are calculated assuming a linear relation with the rainfall intensity (Li, 1979; Sharma et al., 1993, 1995; Gao et al., 2003) as follows:

$$D_{rdd,k} = \alpha_{d,k} r (1-\varepsilon) f_d g_k \qquad D_{rdrd,k} = \alpha_{rd,k} r \varepsilon f_d f_k \tag{7}$$

with:

$$f_d = \left(\frac{z_m}{\max(h, z_m)} \right)^{0.8} \qquad \varepsilon = \min\left(\frac{M_s}{M_{s,cr}}, 1 \right) \tag{8}$$

where the rainfall rate r is given in m/s, $\alpha_{d,k}$ and $\alpha_{rd,k}$ ($kg/m/m^2$) are the rainfall erodibility coefficients for each particle class in the original soil matrix and in the loose sediment layer respectively, ε is a shield factor that represents the protection effect that the loose sediment layer exerts over the original soil layer, and f_d is a rainfall damping factor that accounts for the dissipation of rainfall energy through the water column (Hong et al., 2016; Naves et al., 2020).

The shield factor ε is assumed to vary linearly between 0 and 1 with the total mass of sediment per unit surface in the loose sediment layer (M_s), and it takes the same value for all the particle classes (Fig. 2). When M_s achieves a critical threshold ($M_{s,cr}$) the protection effect is maximum ($\varepsilon = 1$), and no sediment is eroded from the original soil matrix (i.e. $D_{rdd,k} = D_{fdd,k} = 0$).

The rainfall damping factor f_d also varies between 0 and 1 (Fig. 2). If the water depth is smaller than a given user-defined threshold (z_m) there is no rainfall damping (i.e. $f_d = 1$ if $h \leq z_m$). For larger depths it decreases exponentially with the water depth (Fig. 2).

This kind of formulations for rainfall driven erosion, with slightly different implementations of the rainfall damping factor, have been used in previous studies (Cea et al., 2016; Gao et al., 2003; Naves et al., 2020; Nord and Esteves, 2005; Sharma et al., 1995; Shaw et al., 2006; Uber et al., 2021).

The flow driven detachment rate represents the transfer of sediment particles from the original soil matrix to the water column due to bed shear stress, and it is computed for each sediment class as (Foster et al., 1995):

$$D_{fdd,k} = K_{d,k} \max\left(\tau - \tau_s, 0\right) (1-\varepsilon) g_k \tag{9}$$

where $K_{d,k}$ is the flow driven detachability for each particle class expressed in kg/s/N, τ is the bed shear stress and τ_s is the critical bed shear stress of the original soil matrix. The flow driven detachability and the critical bed shear stress are model parameters to be defined by the user, while the bed friction is computed with an empirical

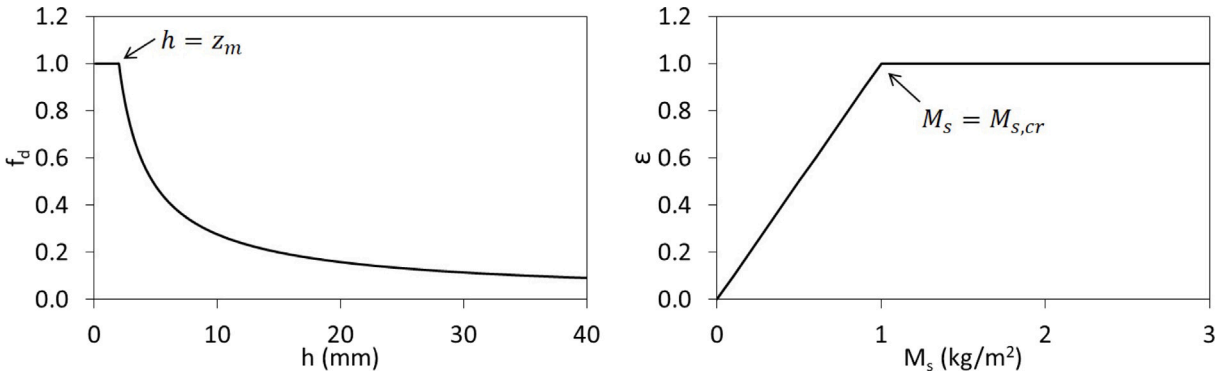

Fig. 2. Rainfall damping factor (left) and shield factor (right) used to compute the rainfall driven detachment and redetachment rates.

formulation (e.g. Manning) when solving the 2D-SWE. The flow driven detachment is also modulated by ϵ and g_k, similarly to the rainfall driven detachment.

The flow driven redetachment of sediment particles from the loose sediment layer into the water column is modelled with Hairsine formulation as (Hairsine and Rose, 1992a,b):

$$D_{fdrd,k} = \frac{\rho_s F_k}{(\rho_s - \rho)\, g} \left(\frac{\Omega - \Omega_0}{h} \right) \epsilon f_k \tag{10}$$

where Ω is the stream power of the flow expressed in W/m^2, Ω_0 is the critical stream power below which the redetachment rate is zero, and F_k is the fraction of stream power used for the redetachment of particles from the loose sediment layer into the water column.

Finally, the deposition of suspended sediment into the eroded layer is modelled as:

$$D_{dep,k} = -\rho_s w_{s,k} C_k \tag{11}$$

where $w_{s,k}$ is the effective settling velocity of the sediment particles of class k. Several formulations can be used to compute the settling velocity of a spherical particle in still water as a function of its density and diameter. We have used for that purpose the formulation of van Rijn (1984).

$$w_{s,k} = \begin{cases} \dfrac{Rg D_k^2}{18\nu} & \text{if} \quad D_k \leq 10^{-4} \text{ m} \\ \dfrac{10\nu}{D_k} \left(\sqrt{1 + \dfrac{Rg D_k^3}{100\nu^2}} - 1 \right) & \text{if} \quad 10^{-4} \text{ m} < D_k \leq 10^{-3} \text{ m} \\ 1.1 \sqrt{Rg D_k} & \text{if} \quad 10^{-3} \text{ m} < D_k \end{cases} \tag{12}$$

However, in practical applications the water is not still, and the sediment particles can interact with each other, both factors affecting their settling velocity. Thus, the effective settling velocity depends on the suspended sediment concentration, flocculation, turbulence intensity and infiltration rate through the soil, and might even be used as a calibration parameter (Tromp-van Meerveld et al., 2008).

2.4. Bed load

The bed load transport capacity for each particle class ($q_{b,k}$ expressed in m^2/s) is computed as:

$$q_{b,k} = q^*_{b,k} \sqrt{\frac{\rho_s - \rho}{\rho} g D_k^3} \epsilon f_k \tag{13}$$

where $q^*_{b,k}$ is the dimensionless bed load transport capacity, which can be computed with any empirical formulation. The following well-known formulations are implemented in the model: Meyer Peter-Müller, Wong-Parker, Einstein-Brown, van Rijn, Engelund-Hansen, Yalin and Ashida-Michiue (Garcia, 2006).

Most of these empirical formulations include a critical shear stress that depends on the particle diameter, and might therefore have a different value for each sediment class. Moreover, its value depends on the presence of other particle classes in the mixture. This interaction between particles of different size is considered in the model as (Garcia, 2006):

$$\tau_{c,k} = \tau_c \frac{D_k}{D_m}^{1-\gamma} \tag{14}$$

where $\tau_{c,k}$ is the critical shear stress of particle class k, τ_c is the critical shear stress corresponding to the mean diameter of the mixture, D_m is the mean diameter of the mixture and γ is the so-called *hiding factor*, which varies between 0 and 1, and controls the interaction between particles of different size. If $\gamma = 1$, the critical shear stress takes the same value for all sediment classes (i.e. there is a maximum interaction or hiding). A value of $\gamma = 0$ recovers the no-interaction hypothesis, in which case the critical shear stress varies linearly with the particle diameter.

2.5. Soil erosion

Once the suspended load and bed load are computed, the following mass conservation equation is solved to compute the time evolution of each particle class in the loose sediment layer:

$$\frac{\partial M_{s,k}}{\partial t} = -\left(D_{rdrd,k} + D_{fdrd,k} + D_{dep,k} \right) - \rho_s \left(\frac{\partial q_{bx,k}}{\partial x} + \frac{\partial q_{by,k}}{\partial y} \right) \tag{15}$$

Notice that only the terms involving the transfer of sediment from or to the loose sediment layer (Fig. 1) are considered in Eq. (15). The total mass of sediment and the mass fraction of sediment particle class are updated as:

$$M_s = \sum_{k=1}^{N_p} M_{s,k} \qquad f_k = \frac{M_{s,k}}{M_s} \tag{16}$$

Lastly, the evolution of the bed elevation is computed from the following mass conservation equation, which includes all the terms implying transfers of sediment particles from or to the loose sediment layer and the original soil layer:

$$\frac{\partial z_b}{\partial t} = -\sum_{k=1}^{N_p} \frac{D_{rdd,k} + D_{rdrd,k} + D_{fdd,k} + D_{fdrd,k} + D_{dep,k}}{(1-\phi)\,\rho_s} - \sum_{k=1}^{N_p} \frac{1}{(1-\phi)} \left(\frac{\partial q_{bx,k}}{\partial x} + \frac{\partial q_{by,k}}{\partial y} \right) \tag{17}$$

At each time step the new bed elevation computed from Eq. (17) is updated in the 2D-SWE to ensure an appropriate coupling between the overland flow and soil erosion.

2.6. External forcings and boundary conditions

The hydrodynamic and soil erosion equations must be provided with appropriate boundary conditions and external forcings in order to be solved.

In rainfall-runoff applications at the catchment or hillslope scales, rainfall intensity is the main external forcing. It might be provided by the user either as spatially variable raster fields for each time step, or as time series at specific rain gauge locations. In both cases the rainfall is interpolated to the elements of the computational mesh. This provides a temporally and spatially variable rainfall field that is included as a source term in the mass conservation equation (source term r in Eq. (1)) and used to compute the rainfall driven detachment and redetachment rates in the suspended sediment transport equation (source terms D_{rdd} and D_{rdrd} in Eq. (7)).

When applying the model at the river reach scale, the main forcings are the inlet discharges of water and sediment at the upstream boundary. The inlet hydrograph and sedigraph (or alternatively the depth-averaged sediment concentration) along the upstream boundary must be provided by the user. Assuming that the friction slope is uniform along the inlet boundary, the total discharge is distributed along the inlet length as:

$$q_{bnd} = K\frac{h^{5/3}}{n} \qquad K = \frac{Q_{in}}{\int_{\Gamma_{bnd}} \frac{h^{5/3}}{n} dL} \tag{18}$$

where q_{bnd} is the unit discharge along the inlet boundary, Q_{in} is the total inlet discharge through that boundary, Γ_{bnd} is the contour of the inlet boundary, and n is the Manning coefficient along the boundary.

At the outlet boundaries, only the water depth must be prescribed. This can be done either as a user-defined water level or as a supercritical flow condition. The former one is applied when the flow at the boundary is subcritical, while the latter one is appropriate when the boundary flow is supercritical. Typically, in mild slope reaches the water level at the outlet boundary is prescribed. However, for steep slope river reaches, or at the catchment and hillslope scales, a supercritical flow condition is in general more convenient.

3. Numerical solver

3.1. Numerical schemes

The 2D-SWE (Eqs. (1)–(3)), as well as the sediment transport Eqs. (6), (15) and (17) are solved with a finite volume solver for unstructured grids. Numerical details of the finite volume method applied to the 2D-SWE and other transport equations are extensively described in the scientific literature. The reader is referred to LeVeque (2002) and Toro (2001, 2009) and the references therein.

In the solver presented here two different numerical schemes were implemented for the discretisation of the convective terms in the 2D-SWE: a Godunov-type scheme based on the approximate Riemann solver of Roe (Toro, 2001) and the DHD scheme (Cea and Bladé, 2015). Numerical details about the specific implementation of the solver of Roe used in this work can be found in Cea et al. (2010), while the description and validation of the DHD scheme is presented in Cea and Bladé (2015). Even if both schemes can be used to solve the 2D-SWE, the scheme of Roe is more efficient and accurate in the presence of shock waves, providing accurate and stable results at the river reach scale (Cea et al., 2007). Meanwhile, the DHD scheme provides more stable and rapid results in rainfall-runoff applications at the catchment and hillslope scales (Cea et al., 2022; García-Alén et al., 2022; Sanz-Ramos et al., 2021). In both cases the bed friction is discretised with a semi-implicit scheme in order to enhance the numerical stability of the solver (Cea and Vázquez-Cendón, 2012).

The suspended sediment transport equation is solved using the explicit finite volume scheme for scalar transport equations described in Cea and Vázquez-Cendón (2012), which ensures the conservation of the mass of sediment. The main particularity of Eq. (6) with respect to a typical scalar transport equation are the source terms, namely $D_{rdd,k}, D_{rdrd,k}, D_{fdd,k}, D_{fdrd,k}, D_{dep,k}$. In order to guarantee the positiveness of the suspended sediment concentration, special care must be taken with the discretisation of the deposition rate ($D_{dep,k}$), since it is the only negative source term in Eq. (6). For this reason, the solver implements an implicit discretisation of the deposition rate that guarantees the positivity of the suspended sediment concentration and the conservation of mass. At the same time, the rainfall and flow-driven redetachment rates (D_{rdrd} and D_{fdrd}) are limited to the availability of sediment in the loose sediment layer, to prevent negative values of the mass of sediment in Eq. (15), while the detachment rates (D_{rdd} and D_{fdd}) are limited to the availability of sediment in the original soil layer.

Most of the applications of the soil erosion model imply the presence of dry regions in the computational domain. The numerical discretisation ensures the conservation of the mass of water and sediment even in the presence of wet–dry fronts. Nevertheless, for computational efficiency, a wet–dry tolerance parameter is defined, such that if the water depth in a computational cell is below this tolerance the cell is considered dry. The numerical treatment of wet–dry fronts is described in detail in Cea et al. (2010), and follows the discretisation proposed originally by Brufau et al. (2004).

3.2. GPU implementation

The standard version of Iber was developed in Fortran following a single-threaded programming model. This makes it easier to develop and debug than programmes using a parallel programming model (Sutter and Larus, 2005; Belikov et al., 2013). However, this approach has significant limitations in terms of computational efficiency, since modern hardware offers most of its computational capabilities through parallel resources (Sutter, 2005; Garland et al., 2008). The single-threaded programming model restricts the efficiency and spatial resolution of the model in applications covering large domains or requiring a large number of simulations (e.g. sensitivity analysis and calibration). In order to overcome the limitations in terms of computation time, it is necessary to exploit the parallelism available in the current hardware architectures through High Performance Computing (HPC) techniques.

One popular and cost-efficient solution in recent years is to use Graphical Processing Unit (GPU) computing. GPUs are designed with massive-parallel architectures, within the order of thousands of processing cores that can work in parallel. This provides a substantial amount of computational power, especially when compared to consumer Central Processing Units (CPU) (Sun et al., 2019). Their capabilities make GPUs suitable not only for graphics but also for many other computing-intensive applications like numerical modelling (Michalakes and Vachharajani, 2008; Grand et al., 2013; Le et al., 2015; Domínguez et al., 2021), where they are referred to as General Purpose Graphical Processing Units (GPGPU). GPU computing technology is available in a wide range of environments: from laptops to HPC data centres, and can be adapted to a wide range of use cases, from prototyping to executing large simulations. In recent years, they have been applied to many hydrodynamic codes based on the 2D-SWE, showing speed-ups of two orders of magnitude (Vacondio et al., 2017; García-Feal et al., 2018; Xilin et al., 2019; Carlotto et al., 2021; Morales-Hernández et al., 2021; Buttinger-Kreuzhuber et al., 2022), as well as other environmental models for rivers (Carlotto et al., 2019; García-Feal et al., 2020; Sanz-Ramos et al., 2023).

In order to address the limitations in computational efficiency of the single-threaded implementation of Iber, a new object-oriented implementation of the solver was developed in C++ and Nvidia CUDA (Compute Unified Device Architecture) (NVIDIA, 2023) employing HPC

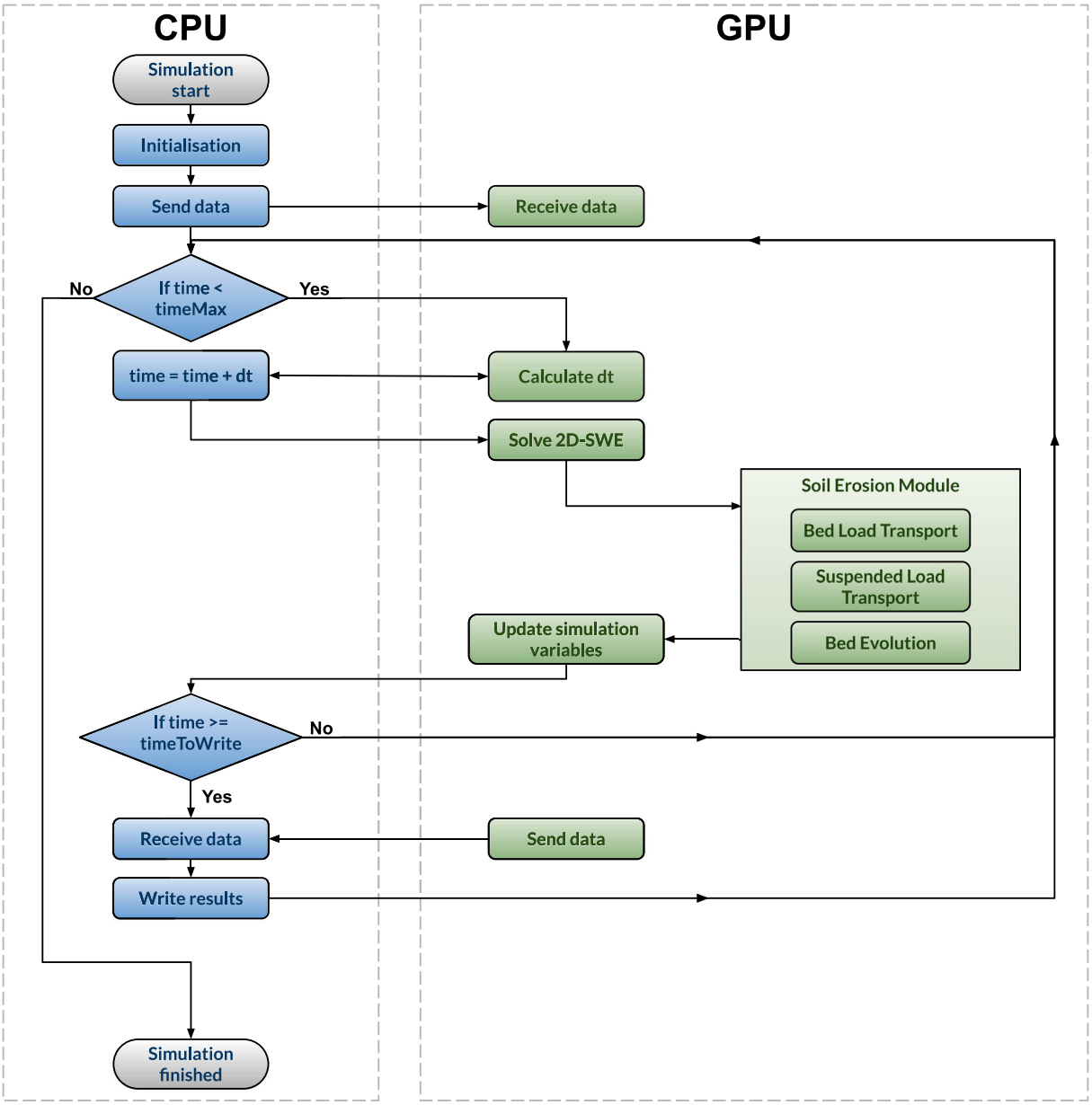

Fig. 3. Flow chart of the GPU implementation.

techniques to leverage GPU computing capabilities. This new implementation, named Iber+, can achieve speed-ups of two orders of magnitude when compared with the non-parallelised version (García-Feal et al., 2018). Both implementations can be used on GNU/Linux as well as on Microsoft Windows systems, and are freely available to download from its official website (https://www.iberaula.com). The initial version of Iber+ offered only the parallelisation of the hydraulics and hydrology modules, later implementing a water quality module (García-Feal et al., 2020). Following the same strategy, the new soil erosion module was parallelised on GPU.

Parallel programming, and especially GPGPU programming presents certain challenges that must be considered when developing software for these platforms. In GPUs, synchronisations between execution threads are expensive, especially global synchronisations that involve a large number of threads. This implies that certain algorithms must be rewritten to avoid or reduce the number of synchronisation operations. To assist with this task, Nvidia provides libraries such as CUB (CUDA Unbound) (Merrill, 2013) that offer generic high-performance parallel implementations for operations like reductions or scans. Even though some algorithms that require many synchronisations can be faster on a CPU than on a GPU, it should be noted that GPUs have their own high-bandwidth memory to support the massive parallelism. However, memory transfers from the regular CPU system memory to the GPU memory are usually bottle-necked by the PCI (Peripheral Component Interconnect) bus. It is therefore advisable to minimise these memory transfers, sometimes even performing some tasks on the GPU that could be faster on the CPU, just to avoid costly memory transfers that would reduce the overall performance.

All these issues were considered in the GPU implementation of the soil erosion module in order to optimise its computational performance. The execution flow chart of the Iber+ code is shown in Fig. 3. Once the input data is read and the simulation is initialised on the CPU, the data is transferred to the GPU memory and the main computation loop starts. The CPU controls the main loop, responsible for launching GPU computations and incrementing the time counter of the simulation. In this way, for each computational time step, the memory transfers are minimised to a single variable, i.e. the current simulation time step. Only at time steps when it is necessary to write results to the output

Table 1
Test cases used to show the performance of the soil erosion model.

Test case	Spatial scale	Area (m2)	Mesh elements	Forcing	Rainfall spatial variability	Type of transport	Sediment classes	Analysed variables	Approach
T1	Laboratory	12	120	Rainfall	No	Suspended load	7 particle sizes	Q(t), Qs(t)	Experimental validation
T2	Hillslope	120	3300	Rainfall	No	Suspended load	1	Q(t), Qs(t)	Field validation
T3	Catchment	2.00E+07	94 119	Rainfall	Yes	Suspended load	4 spatial origins	Qs(t)	Sensitivity to rainfall variability
T4	River reach	1.23E+07	45 314	Discharge	NA	Bed load	1	Zb(t)	Field validation

files, the data is transferred back to CPU memory. The output files are written to disk by the CPU in a background thread, while the simulation continues running on the GPU.

4. Model application and validation

This section presents four test cases that cover different potential applications of the soil erosion model described in the previous sections, ranging from the laboratory scale to the catchment scale (Table 1).

The mathematical formulations described above require a detailed definition of several parameters and soil properties. Many of these parameters are difficult to measure, and their calibration with field data in practical applications is complex due to the scarcity of comprehensive field data available for calibration, the uncertainty in field measurements and input data, the high non-linearity of the model equations, the interaction between input parameters, and the high spatial and temporal variability of the physical processes involved in soil erosion. All these contribute to the well-known equifinality problem in hydrological and soil erosion modelling (Beven, 2006; Vrugt et al., 2009), implying that several combinations of the input parameters can produce a similar model output. Therefore, it is complex to calibrate and run a soil erosion model including all the available processes and parameters. Instead, simplifications must be done in order to include the most relevant processes in such a way that the number of input parameters and calibration efforts are reduced (Cea et al., 2016). This task relies on the modeller and depends on the specific case study, as well as on the availability of input and calibration data. In this context, *model configuration* is understood as the selection of processes, formulations and parameterisations used in a specific case study. The number of possible model configurations is huge and the four test cases included in this section are just intended to illustrate some relevant potential applications of the model by focusing on different soil erosion processes.

In the first test case the model is validated against the experimental results of soil erosion in a 6 m long and 2 m wide laboratory flume presented by Tromp-van Meerveld et al. (2008). Model output is compared with the observed time series of sediment flux for seven size classes, in order to assess its capability to represent size-selectivity processes at the laboratory scale. The second case presents the application of the model to a plot of 60 x 2.2 m (132 m^2) located on a hillslope with vineyards cultivated in the slope direction. Solid and liquid discharges measured at the terrain outlet during 4 rainfall events are used to calibrate and validate the model. The third case study is a headwater mountain catchment of 20 km^2 located in the French Alps, and it is used to show the sensitivity of the solid discharge computed at the basin outlet to the spatial variability of rainfall. The last test case shows the capability of the model to compute bed load transport and morphological changes at the river reach scale, using for that purpose the observed effects of the debris flood that occurred on the Ullion creek (France) during the storm Alex, in October 2020.

4.1. Multiclass rainfall driven erosion in a laboratory flume

Tromp-van Meerveld et al. (2008) conducted a series of rainfall driven soil erosion experiments in a 6 m long and 2 m wide rectilinear flume. The bed of the flume was made of a sediment mixture with grain sizes ranging from clay to sand. Time series of sediment concentration for seven size fractions (<0.002, 0.002–0.020, 0.020–0.050, 0.050–0.100, 0.100–0.315, 0.315–1.0 and >1.0 mm) were measured at the flume outlet, and will be used here to compare with the predictions of the numerical model. The proportion of these seven particle classes in the original soil (g_k) varies within 0.075 for the coarsest fraction and 0.225 for the finest ones (Table 2). Here, we used the conditions of experiment H3, in which the slope of the flume was 2.2% and a rainfall intensity of 47.5 mm/h was imposed during 2 h. Infiltration was estimated to be 3.2 mm/h by the authors of the experiments. Rill formation was not observed during the experiments, suggesting that rainfall-driven erosion was the only relevant erosion mechanism.

This experiment was reproduced numerically by Tromp-van Meerveld et al. (2008) using an analytical solution of the Hairsine–Rose erosion model that assumes steady state and spatially uniform hydraulic conditions. Several calibration alternatives were considered in their work, the main conclusion being that, in order to correctly reproduce the sediment concentration of all classes at the flume outlet, the settling velocity of each size class had to be adjusted individually. Tromp-van Meerveld et al. (2008) give a number of possible reasons why adjusting the settling velocity is necessary, including: (1) the formation of aggregates of clay and silt (flocculation) with a larger settling velocity than the individual particles; (2) shallow water depths of the order of a few mm that prevent the largest particles from reaching their final settling velocity; (3) hindered settling due to high sediment concentrations (Baldock et al., 2004); (4) the effect of turbulence on the settling velocity (Kawanisi and Shiozaki, 2008; Pasquero et al., 2003); (5) a higher infiltration rate at the beginning of the experiment leading to a larger settling velocity for the smallest particles and; (6) errors in the measurement of the particle size distribution of the original soil. Most of these effects would tend to increase the theoretical settling velocity of the smallest fractions and to reduce the settling velocity of the largest fractions.

For modelling purposes, in this work we have discretised the rectilinear flume with 5 cm long and 2 m wide rectangular elements (in whole, 120 mesh elements). This is equivalent to a 1D mesh with a grid size of 5 cm. Since water depth data is not available to calibrate the bed roughness, the Manning coefficient was fixed to $n = 0.020$ s $m^{-1/3}$, which is a consistent value for a flat bed with a 1 mm grain size. A critical depth boundary condition was imposed at the flume outlet and the only external forcing was a constant and uniform rainfall intensity of 47.5 mm/h during two hours. The infiltration rate was fixed to a constant value equal to the measured one, i.e. 3.2 mm/h.

Regarding the configuration of the Iber soil erosion model, the seven size classes that were measured in the experiments were considered (Table 2). Following a similar approach as in Tromp-van Meerveld et al. (2008), only suspended load and rainfall driven erosion were considered in the model, and the rainfall detachment and redetachment erodibility coefficients were assumed to be constant for the seven size classes (i.e. $\alpha_{d,k} = \alpha_d$ and $\alpha_{rd,k} = \alpha_{rd}$ for all particle classes k). Due to the small water depths in the flume (of the order of 1–2 mm), it was assumed that rainfall damping was negligible and thus, the rainfall damping factor was fixed to one ($f_d = 1$). On the other hand, the critical mass in the eroded layer ($M_{s,cr}$) was manually calibrated. This

Table 2
Particle classes considered to model experiment H3 in Tromp-van Meerveld et al. (2008).

Class (k)	Size (mm)	g_k	D_k (mm)	$w_{s,k}$ (mm/s)	$w_{s,eff}$ (mm/s)	Correction factor	Correction factor in Tromp-van Meerveld et al. (2008)
1	<0.002	0.225	0.001	0.001	0.003	4.0	3.5
2	0.002–0.020	0.225	0.011	0.11	0.54	5.2	4.5
3	0.020–0.050	0.125	0.035	1.07	25.07	23.5	9.0
4	0.050–0.100	0.125	0.075	4.90	58.05	11.8	8.5
5	0.100–0.315	0.125	0.208	26.48	70.77	2.7	15.0
6	0.315–1.0	0.100	0.658	87.46	70.77	0.8	0.7
7	>1.0	0.075	1.0	137.74	70.77	0.5	0.4

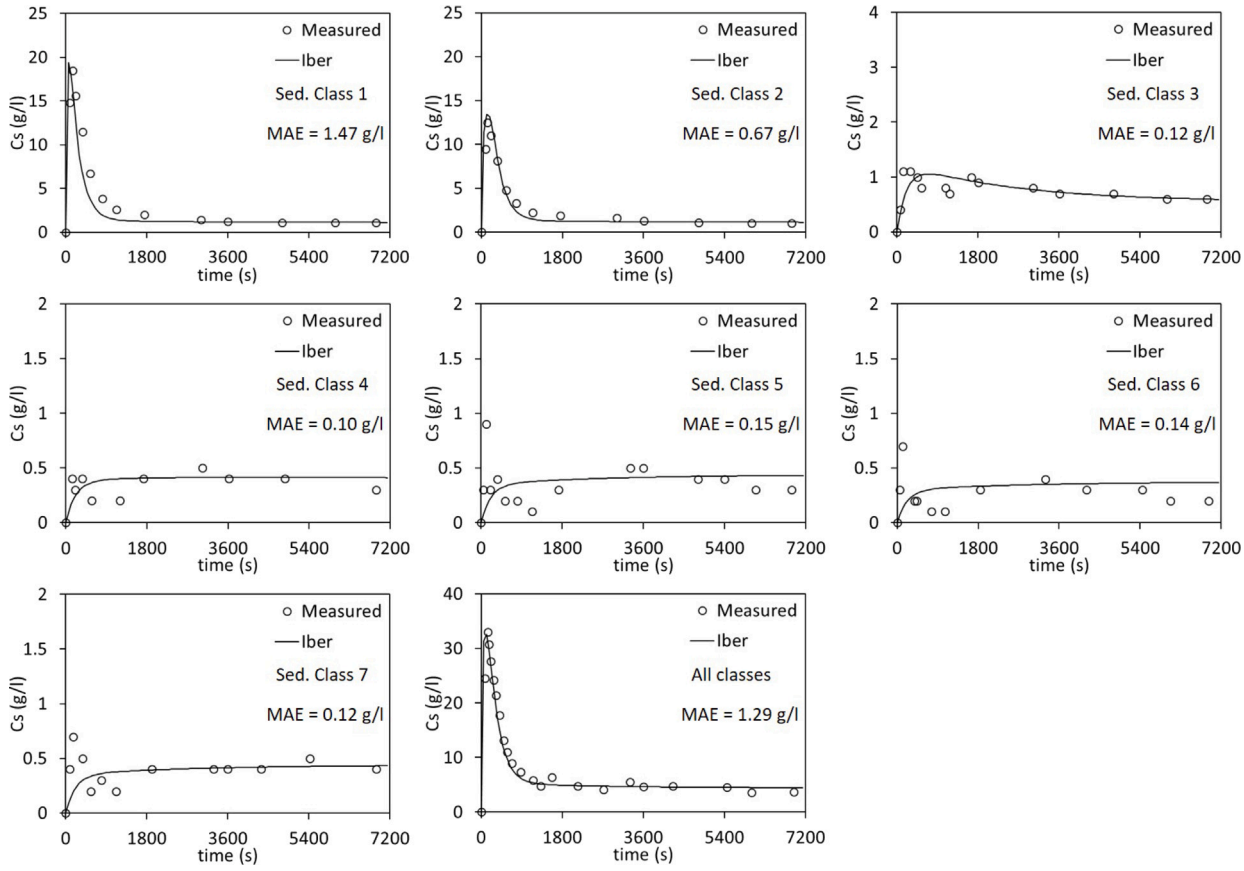

Fig. 4. Computed and measured (Tromp-van Meerveld et al., 2008) time series of sediment concentration at the laboratory flume outlet.

parameter has a significant influence in the results, since it is used to compute the shield factor (ϵ) in Eq. (8), and it controls the initial concentration peak in the sedigraphs of the smallest size classes.

The values of the three previous parameters were manually calibrated to $\alpha_d = 100$ g/m^2/mm, $\alpha_{rd} = 10\,000$ g/m^2/mm and $M_{s,cr} = 0.13$ kg/m^2. In addition, for the reasons given in Tromp-van Meerveld et al. (2008) and mentioned above, it was necessary to adjust the settling velocity of each sediment class in order to correctly reproduce the observed time series of suspended concentration for the seven classes (Fig. 4). The adjusted settling velocities, as well as the correction factors defined as the ratio between the effective and theoretical settling velocity (the latter one computed with the formula of van Rijn (van Rijn, 1984)), are shown in Table 2. The correction factors are larger than one for the five smallest sediment classes, and smaller than one for the two largest sizes. Notice also that the effective settling velocities for the three largest sizes are the same. These results are consistent with those of Tromp-van Meerveld et al. (2008), although the correction factors are slightly different, as shown in Table 2.

With the previous parameterisation the model achieves good agreement with the experimental data. The sedigraphs obtained with the numerical model have shown Mean Absolute Errors (MAE) ranging from 5% to 20% of the peak concentration for each sediment class when compared with the observed sedigraphs (Fig. 4). Additionally, the global trend of the concentration time series is also properly captured for the seven classes as shown in Fig. 4. The model was specially accurate in estimating the peak concentration for the smallest fractions while encountering more difficulties in reproducing the larger fractions. For the total concentration time series, the MAE was 1.22 g/l, for a maximum concentration of 33 g/l, which represents a relative error of 4%, showing that overall, the model was able to reproduce the observed data.

4.2. Rainfall and runoff driven erosion at the hillslope scale

In the second test case the model was applied to a Mediterranean hillslope vineyard of 130 m^2 located in Ardèche (south eastern France), which is part of the Olivier de Serres site of the Cévennes – Vivarais Mediterranean Hydrometeorological Observatory (OHMCV) (Boudevillain et al., 2011). The hillslope is 60 m long and 2.2 m wide. Its topography was measured at 15 cross sections and 6 points per cross

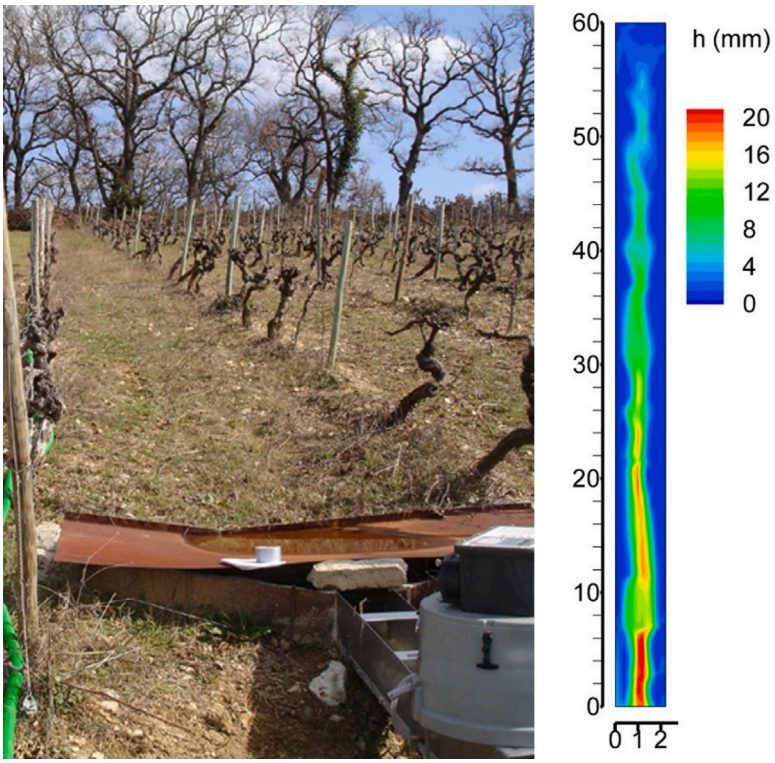

Fig. 5. Hillslope vineyard (left) and typical water depth pattern during a storm event (right) in test case 2.

section, with an uncertainty of 1 cm in the three dimensions. The average longitudinal slope is around 15%, and there is a natural rill that conveys all the surface runoff to the foot of the hillslope, with no runoff losses through the lateral sides (Fig. 5). The soil is calcareous and covered by sparse vegetation, with an approximate composition of 34% clay, 41% silt and 25% sand.

The soil erosion data monitored during the four storm events included in Table 3 were used to calibrate and validate the model. These data sets and the Digital Elevation Model (DEM) of the vineyard are described in detail and can be downloaded from Nord et al. (2017). Rainfall was measured with a raingauge located at the downstream end of the hillslope. The outlet discharge was measured continuously with an H-flume located at the downstream outlet. The concentration of sediment at the outlet was estimated from water samples taken within the H-flume using an automatic sampler. Samples were taken only when predefined thresholds of water discharge or discharge variations were exceeded. Thus, depending on the storm event, between 11 and 21 sediment concentration measurements were done. Specific details about the instrumentation and experimental procedure can be found in Grangeon (2012) and Nord et al. (2017).

The maximum 1-minute rainfall intensity in the storm events analysed varies within 24 and 92 mm/h, while the outlet discharge varies between 0.30 and 1.73 l/s, and the maximum suspended sediment concentration between 0.18 and 1.42 g/l.

In the numerical model the hillslope was discretised with a structured mesh and a uniform cell size of 0.20 m (3300 mesh elements). Given the small size of the hillslope, all the numerical parameters and input data were assumed to be uniform in space. Considering that the average slope in the longitudinal direction is about 15%, and the configuration of the H-flume located at the hillslope outlet, a critical depth condition was imposed at the downstream boundary. The inlet discharge at the upstream boundary was zero, and the only external forcing was the rainfall intensity measured by the raingauge, which was imposed in the model with a rainfall depth resolution of 0.2 mm. As mentioned above, the surface runoff is confined in the transverse direction by the topography, preventing any water or sediment fluxes through the lateral boundaries.

The bed roughness was characterised with the Manning coefficient, and its value was calibrated manually for each event, since the macro-roughness of the hillslope (including vegetation) varies from one season to another, depending on the tillage. Rainfall losses were estimated with a simple model that consists on an initial abstraction (I_a) and a constant potential infiltration rate (k_s). The initial abstraction is subtracted from the input rainfall, while the infiltration rate is subtracted at each computational time step from the surface runoff depth at each mesh element, as long as the local water depth is enough to satisfy the potential infiltration rate. Regarding soil erosion, a relatively simple model configuration was considered, with a single loose sediment layer of infinite thickness (i.e. unlimited availability) and only two erodibility parameters that control the rainfall and runoff-driven redetachment (F and α_{rd} respectively). Therefore, five input parameters were used to calibrate the model, namely I_a, k_s, n, F and α_{rd}. From these, the three parameters that control the transfer of water (I_a, k_s, n) were allowed to vary from one event to another in order to reproduce as accurately as possible the observed outlet hydrographs, while the two parameters that model the transfer of sediment (F and α_{rd}) were calibrated for the storm event R1 and maintained constant for the other three validation events (Table 4).

The computed and observed hydrographs and sedigraphs at the hillslope outlet are shown in Fig. 6. The agreement between the numerical and observed hydrographs is very good in the four events, suggesting that the surface runoff is correctly reproduced by the model and that the hydraulic variables involved in the runoff-driven erosion are properly predicted. It should be noted that the good agreement between observed and modelled hydrographs was obtained with different parameter values for the four events. The initial abstraction of rainwater and the roughness coefficient varied by a factor of 3 while the infiltration rate varied by a factor of 40. This wide variation in infiltration is consistent with the presence of swelling clay on the site and the regular tillage of the soil in the vineyard, which causes the hydrodynamic properties of the soil to vary greatly over time.

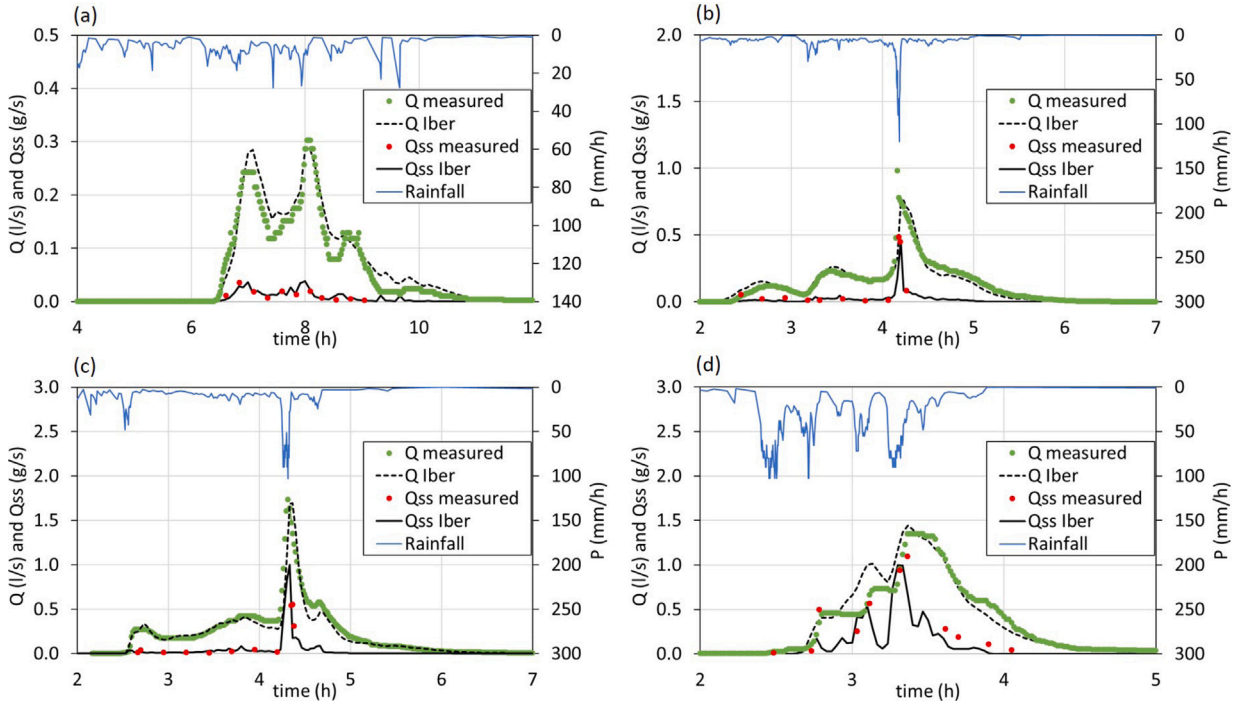

Fig. 6. Numerical and observed outlet hydrographs and sedigraphs for the four rainfall events analysed in the hillslope vineyard (test case T2). Events: (a) R1, (b) R2, (c) R3 and (d) R4.

Table 3
Characteristics of the four storm events in the hillslope vineyard (test case 2).

Event	Start	Max. 1 min rain intensity (mm/h)	Rain depth (mm)	Runoff duration (h)	Runoff depth (mm)	Qmax (l/s)	Cs, max (g/l)
R1	09/11/2012 22:00	24	65	10	12	0.30	0.18
R2	04/11/2011 12:00	79	129	3.9	17	0.98	1.32
R3	18/05/2013 08:00	80	46	5	29	1.73	0.76
R5	20/10/2013 06:00	92	64	2.6	29	1.35	1.42

Table 4
Model parameters and performance results for the four storm events analysed in the hillslope vineyard (test case 2). The performance results refer to the agreement between observed and computed sedigraphs at the hillslope outlet.

Event	n (s/m$^{1/3}$)	I_a (mm)	k_s (mm/h)	α_{rd} (g/m^2/mm)	F ($\times 10^{-3}$)	$MAE/Q_{s,max}$	NSE
R1	0.6	36	1.8	20	0.001	0.10	0.74
R2	0.3	11	1.3	20	0.001	0.04	0.91
R3	0.2	11	0.0	20	0.001	0.09	0.66
R5	0.8	32	0.9	20	0.001	0.13	0.70

Regarding the sedigraphs, using the same erodibility parameters in the four events, the model is able to reproduce the order of magnitude and the time variability of the sediment fluxes, with Nash–Sutcliffe Efficiency (NSE) values ranging from 0.66 to 0.91 and Mean Absolute Errors (MAE) that vary between 4% and 13% of the maximum observed solid discharge for each event (Table 4).

4.3. Spatial variability of rainfall driven erosion at the catchment scale

The aim of this test case is to show the effect of the spatial variability of rainfall at the catchment scale on the modelled water and sediment fluxes at the basin outlet. The soil erosion model was applied to the Galabre basin, a 20 km^2 meso-scale headwater catchment located in the French Alps that is part of the Draix-Bléone Observatory. Liquid and solid discharges are continuously monitored at the catchment outlet (Legout et al., 2021).

The main types of lithologies in the catchment are limestones, marls, molasses and quaternary deposits. Around 10% of the catchment surface is covered by dispersed badlands that constitute the main source of sediment at the basin outlet (Esteves et al., 2019; Poulenard et al., 2012; Legout et al., 2013). The rest of the land is permanently covered by forests and bushes, contributing to a much less extent to the sediment yield.

The numerical discretisation of the basin was done with an unstructured mesh of triangular elements, using different element sizes in the hillslopes, badlands and river network. This approach to building the mesh has the advantage of providing higher spatial resolution in regions where water and sediment fluxes concentrate, i.e. in the river streams and in the badlands. Similar discretisation schemes for solving the 2D-SWE in hydrological applications have been used for instance in Cea et al. (2022), Costabile and Costanzo (2021) and Ferraro et al. (2020). The main river network was defined from a DTM of the catchment with a spatial resolution of 1 m, assuming a Contributing Drainage Area (CDA) of 500 ha to define the perennial water streams, and a CDA of 15 ha to define the intermittent streams composed of small tributaries. The river network obtained using these thresholds is shown in Fig. 7, and it is coherent with *in situ* observations (Uber et al., 2021). The computational mesh was built considering this stream network as well as the location of the badlands shown in Fig. 7.

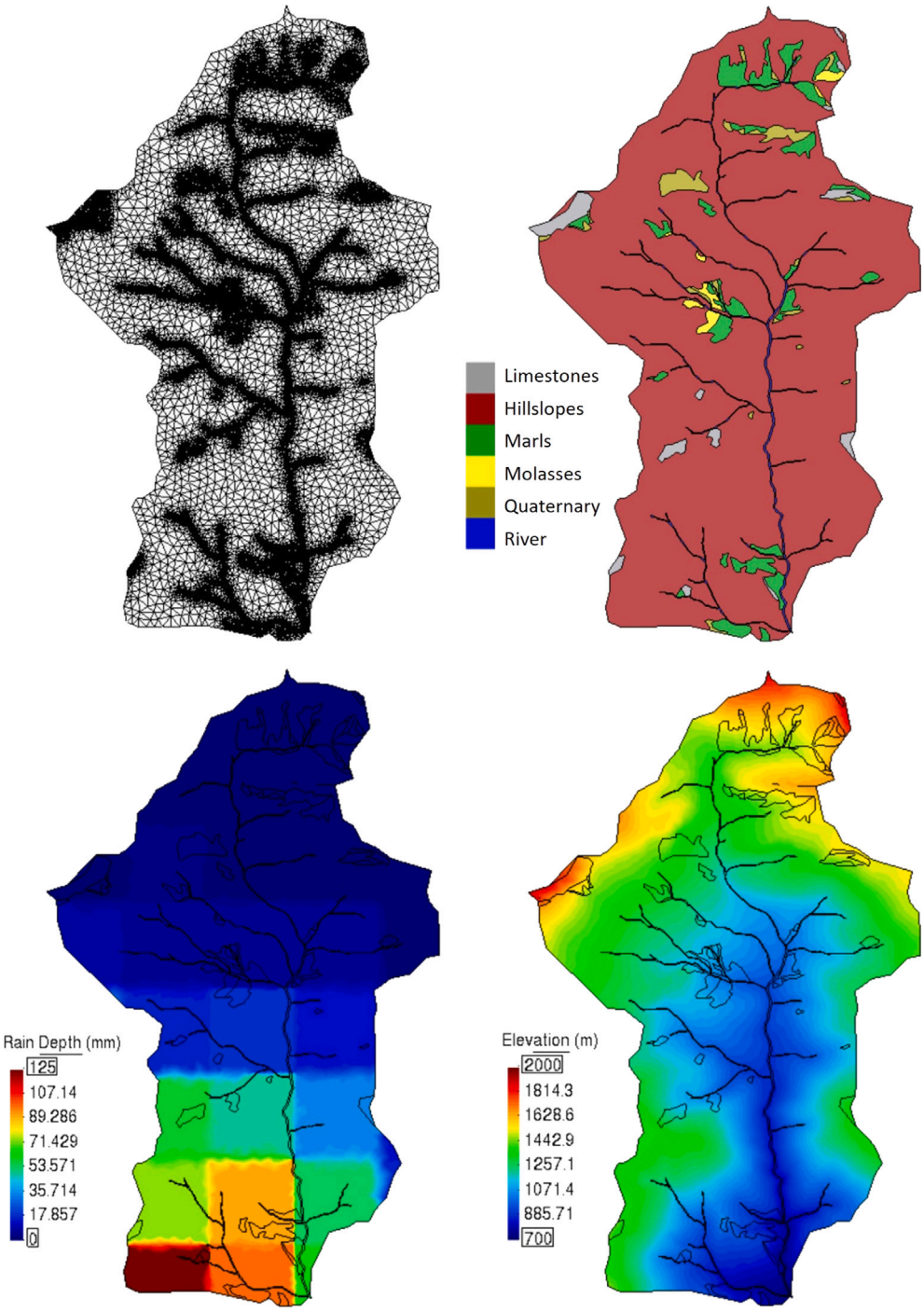

Fig. 7. Galabre catchment. Computational mesh (upper-left), spatial distribution of lithologies (upper-right), spatial distribution of rainfall depth for the 23/06/2010 storm (lower-left) and topography (lower-right).

On the hillslopes, a mesh size of 100 m was used in order to avoid an excessively high number of elements. On the badlands, where the sediment fluxes originate, a mesh size of 20 m was used. The mesh size was refined to 5 m inside a buffer layer along the river network. This buffer layer was 5 m and 10 m wide on both sides of the river network, for the intermittent and the perennial streams respectively. Such widths are consistent with the approximate width of these streams in the catchment. With this discretisation scheme, the number of mesh elements was around 94 000. Following Uber et al. (2021), the Manning bed roughness coefficient was set to 0.05 in the river network and to 0.80 on the hillslopes.

Soil erosion was modelled for a rainfall event recorded on 23/06/2010, prescribing the effective rainfall intensity in two different ways: (1) as spatially distributed rainfall fields defined from raster files with spatial and temporal resolutions of 1 km and 15 min respectively and (2) as spatially uniform rainfall fields defined as the spatial average of the rainfall fields over the entire catchment, with a time resolution of 15 min. Both rainfall products are equivalent in terms of the spatial average of rainfall intensity at each time step. The only difference between both simulations was the spatial variability of rainfall. The spatial distribution of rainfall depth for the entire event over the whole catchment is shown in Fig. 7.

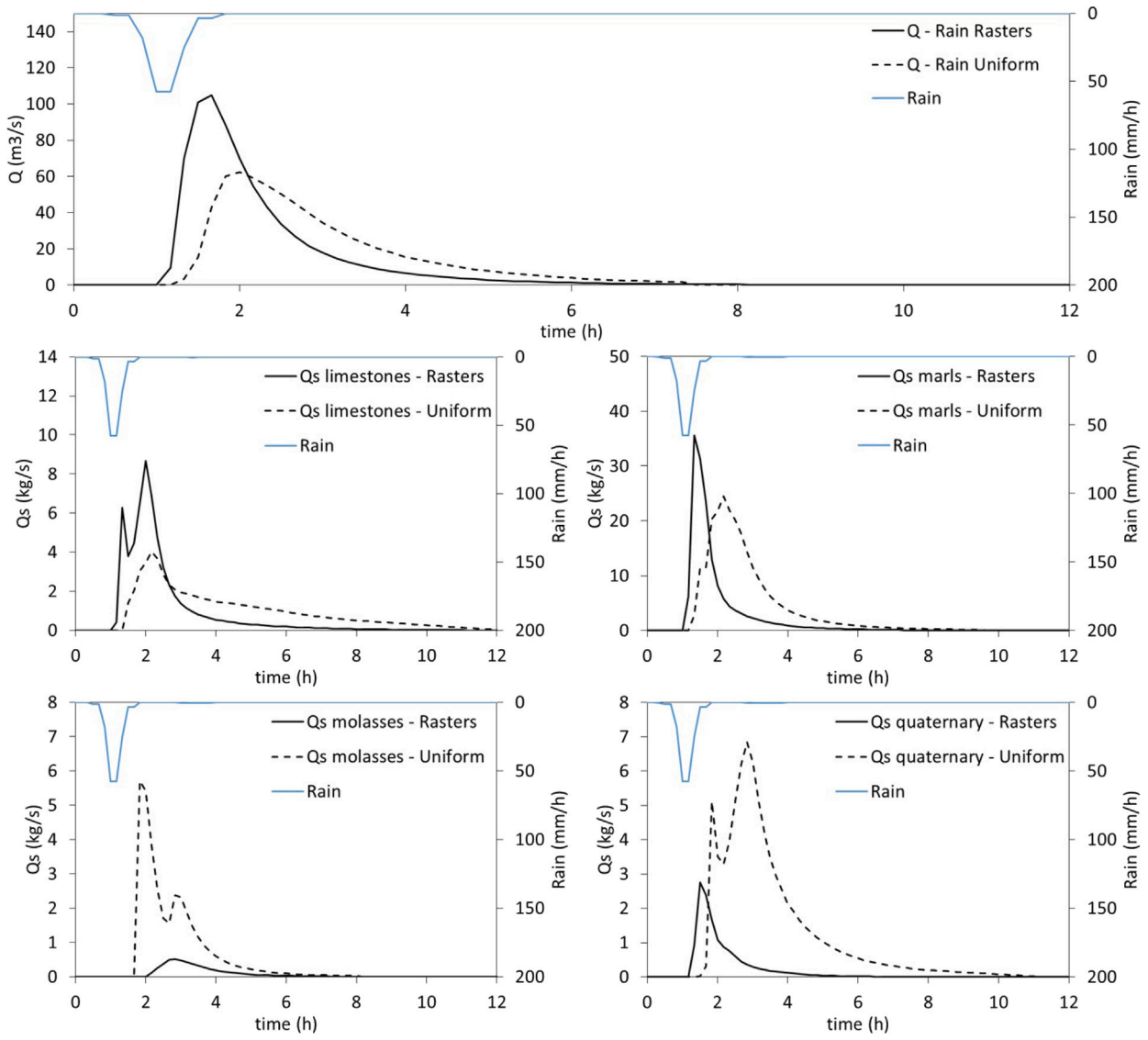

Fig. 8. Hydrographs and sedigraphs computed in the Galabre catchment using spatially uniform and variable rainfall fields.

For modelling purposes, only the rainfall-driven erosion was considered with a single loose sediment layer of infinite thickness (i.e. unlimited availability), and the production of sediment was limited to the badlands. Four different sediment types were defined according to the four lithologies in which the badlands are developed, i.e. limestones, marls, molasses and quaternary deposits (Fig. 7). The rainfall erodibility coefficient was assumed to be the same for all the badlands in order to focus the analysis on the effect of the spatial variability of rainfall. Its value ($\alpha_{rd} = 7.4 \mathrm{g/m^2/mm}$) was taken from Uber et al. (2021), where its average value was estimated from the interannual observed rainfall depth and suspended sediment yield at the catchment outlet.

Fig. 8 shows the relevance of considering the spatial variability of rainfall when modelling soil erosion in this meso-scale catchment. The hydrographs and sedigraphs computed differ significantly between the two scenarios, not only in their peak values, but also in the total sediment yield (Table 5). When assuming a spatially uniform rainfall field the peak discharge diminishes considerably compared to the spatially variable case (from 104.7 to 62.3 $\mathrm{m^3/s}$), since in the former case the rainfall intensity is homogeneously distributed over the entire catchment, instead of being concentrated around the basin outlet, as it is when its spatial variability is considered (Fig. 7). The effect is similar when looking at the fluxes of marls and limestones, which originate from badlands that are more or less distributed all over the catchment. For these two sediment types the peak fluxes are significantly higher when considering the rainfall variability (Table 5). On the contrary, molasses and quaternary deposits are mainly located in the upper part of the catchment and they are eroded at a much lower rate when the spatial variability of rainfall is considered in the model, since the observed rainfall depth was very low in this part

Table 5
Water and sediment fluxes computed in the Galabre catchment with spatially uniform and variable rainfall fields.

Rainfall input	Peak flux ($\mathrm{m^3/s}$ for water and ton/s for solid)				
	Water	Limestones	Marls	Molasses	Quaternary
Uniform	62.3	4.0	25.4	5.7	6.8
Rasters	104.7	8.7	35.6	0.5	2.7
Rainfall input	Total mass flux ($\mathrm{m^3}$ for water and ton for solid)				
	Water	Limestones	Marls	Molasses	Quaternary
Uniform	430 596	39.3	145.9	21.4	47.7
Rasters	449 214	36.5	92.5	3.1	8.2

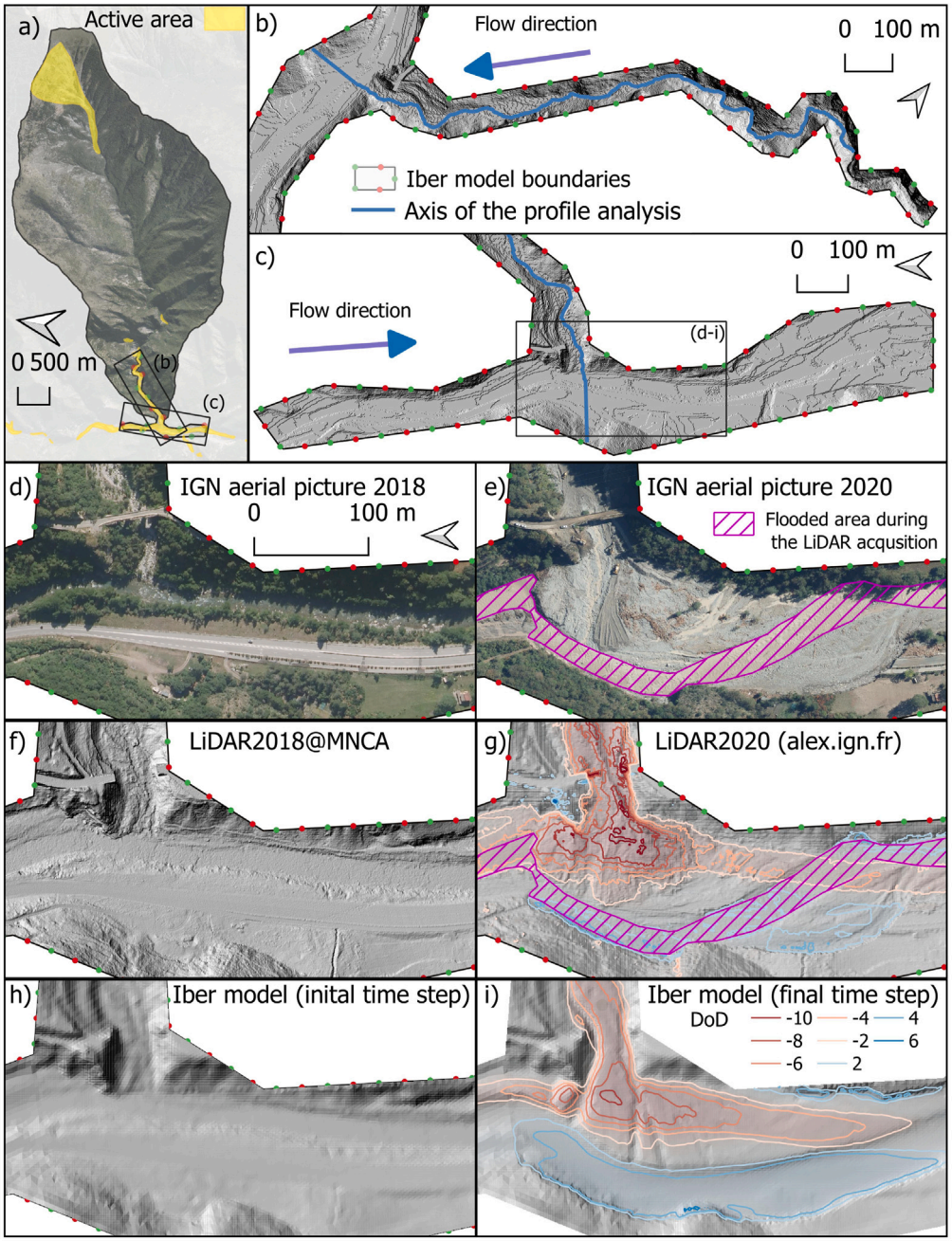

Fig. 9. Ullion catchment case study: (a) general view including the landsliding area in the headwaters and the deposition zone near the confluence; (b) zoom on the extension of the Iber model on the Ullion Creek branch; (c) zoom on the extension of the Iber model on the Tinée River branch; aerial pictures of IGN (d) before and (e) after the event including the hatched area where flow was still high during the LiDAR acquisition and thus the elevation reported is that of the free surface and not of the terrain; DEM digital elevation model (f) before and (g) after the event including coloured contour lines of the DoD (difference between initial and final DEMs); and Iber model bed elevation (h) before and (i) after the event including coloured contour lines of the DoD.

of the catchment. For these two sediment types the peak fluxes are much smaller when considering the spatially variable rainfall field. It is important to note that these simulations were carried out using a simplified representation of erosion, taking into account only the detachment by rainfall. Simulations that take into account the deposition and remobilisation of sediments by the flow on hillslopes and in the hydrographic network could be carried out to fully assess the role of spatio-temporal variability of rainfall on the sediment dynamics of medium-scale catchments.

4.4. Massive bed load deposition during a debris-flood event

The aim of this case study is to demonstrate the capability of the model to correctly reproduce in-channel processes, such as very active bed load transport. An un-published analysis of the Ullion creek debris-flood that occurred during the Alex Storm (2–3 Oct. 2020) exemplifies that the present soil erosion module can also be used to focus solely on river channels (Piton and Rodier, 2022).

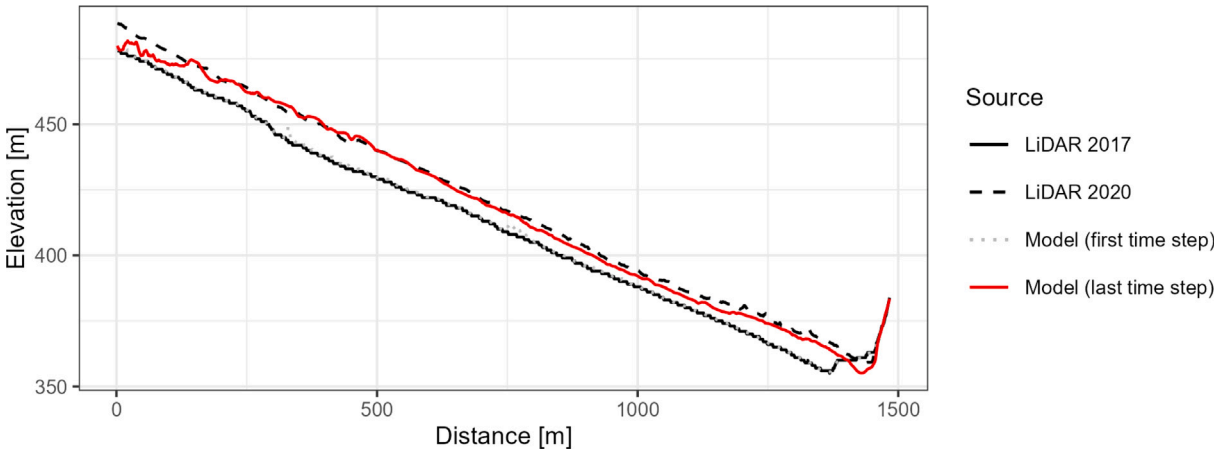

Fig. 10. Longitudinal profile along the axis of the Ullion creek (blue line on Fig. 9b–c) with observed and model bed states.

The Ullion Creek is a tributary of the Tinée River in the south east of France. Its 12 km^2 catchment is very steep, ranging from 2087 m.a.s.l. to 356 m.a.s.l. at the confluence with the Tinée (Fig. 9a). Only the last 1.5 km of this 7.7 km long creek was modelled in this study. The creek channel is confined between steep hillslopes until the confluence (Fig. 9b), and has a very uniform longitudinal slope of 11.0% along the modelled reach (Fig. 10). The Tinée River has conversely a catchment of about 600 km^2 at the confluence. Its river bed shows evidences of regular bedload transport. It has an average longitudinal slope of about 1.1%, and it flows into a valley with an alluvial floodplain located on the right bank (Fig. 9c). Two roads follow the Tinée River axis near the study site, a main road on the right bank in front of the creek and an old road, usually closed, passing the creek on an old bridge (Fig. 9d).

On the 2nd and 3rd October 2020, the Alex Storm hit the region triggering extreme rainfalls and catastrophic floods with astonishingly high sediment transport, erosion and damages to roads, infrastructures and buildings (Carrega and Michelot, 2021; Liébault et al., 2024; Piton et al., 2024). The rainfall estimated from the combination of weather radar and rain gauges was higher than 500 mm on the Ullion Creek catchment within less than 24 h (Brigode, 2021; Payrastre et al., 2022). A large landslide occurred in a former diffuse gullying area and fed suddenly the creek with an unlimited amount of sediment. The sediment was transported mainly as bed load, at least in the downstream part of the basin according to videos taken by local dwellers. A massive deposition occurred in the creek bed, elevating the bed level by about 7 m, on average. An alluvial fan that was formed at the confluence dammed and diverted the main river to the opposite bank, thus resulting in the erosion of about 300 m of the main road (compare Fig. 9d and f with Fig. 9e and g). This case study is well documented as a debris-flood event, i.e. a very intense flood carrying massive amount of bed load material and involving large erosion and/or deposition (Church and Jakob, 2020).

Two DTM where obtained from light detection and ranging (LiDAR) data, the first dating from 2018 (LiDAR2018@MNCA) and the second dating from two days after the event (LiDAR2020@IGN). A total volume of bed material deposit of about 330,000 m^3 was estimated from the difference between both DTM within the extent of the alluvial fan deposit and of the 1.5 km terminal reach of the creek.

The *post*-event LiDAR data is available only for the terminal reach of the creek, so the analysis was focused only on this area. The event hydrographs entering the analysed Ullion creek and Tinée River reaches were reconstructed from the distributed rainfall data, using the Curve Number (CN) method with an hypotheses of flow velocities of 0.2 m/s on hillslopes and of 5 m/s in channels (Brigode, 2021). A value of CN = 60 was taken according to field evidences and back analysis of flood marks performed by Payrastre et al. (2022). The resulting hydrograph for the Ullion catchment lasts about 23 hr, has a peak discharge of 86 m^3/s at 15:00 and a cumulated volume of 2.5 Mm^3. The ratio between the deposited bedload volume and the hydrograph volume is about 0.16, implying a very high concentration for bed load, but not uncommon during debris floods (Church and Jakob, 2020). For the Tinée, the peak discharge is 905 m^3/s and the volume 31.5 Mm^3.

As a first approximation, we assumed clear water flow at the inlet boundaries until the material coming from the landslide reached the model boundary. We then computed the bed load discharge using the Meyer-Peter and Müeller (MPM) equation. The time at which the bedload transport wave reached the model boundary is estimated to be 15:00 ± 1:00 according to a sensitivity analysis and comparison to field observations from the local firefighters (Piton and Rodier, 2022). Grain size samples were measured *a posteriori* with D_{50} = 23 mm in the main body of the deposit. The Manning coefficient of the model was fixed at 0.070 $s\ m^{-1/3}$ assuming a near-critical Froude number, as measured in debris-flood experiments (Piton and Recking, 2019), while in the Tinée a value of 0.045 $s\ m^{-1/3}$ provided reasonable results. Tests performed with 0.04 $s\ m^{-1/3}$ led to too much deposit in the channel while tests performed with 0.05 $s\ m^{-1/3}$ resulted in not enough deposition. A triangular unstructured mesh was used to discretise the spatial domain, with elements of 3 m in the Ullion creek and of 5 m in the Tinée. The total number of elements of the computational mesh was around 45,000. According to our field observations, the bed channel was considered non-erodible in the Ullion Creek. Conversely a 6 m-deep erodible layer was set at the confluence and 2 m-deep further upstream and downstream. These depths were selected higher than the maximum erosion measured between the two LiDAR surveys.

It is worth stressing that 2D numerical modelling including sediment transport is so far considered not mature enough to be used in studies of massive bed load transport in steep creeks, e.g. to assess debris-flood hazards (Jakob et al., 2022). In this case study, despite using the probably most commonly used bed load transport equation in gravel bed rivers, namely MPM, and common values of Manning coefficients, the model provided very satisfactory results. The slope and spatial distribution of the deposit are similar to the observations (Fig. 10), being slightly lower than observed in the final reach. Landforms as channels, terraces and even the alluvial fan appear in the model in a very similar fashion than in the field. The contour lines of the DoDs (differences in DTM) show very similar patterns in the measurement and simulation (Fig. 9g & i): the deposit reached 8–10 m at the mouth of the steep creek and rapidly decreased in a shape of an alluvial fan that was truncated by the main river. The alluvial fan material was indeed partially transported downstream by the river.

Consistently with the longitudinal profile being slightly lower than observed (Fig. 10), the alluvial fan is slightly more extended towards the downstream direction than actually observed (Fig. 9g & i). The extension of the bank erosion that destroyed the road is also reasonably

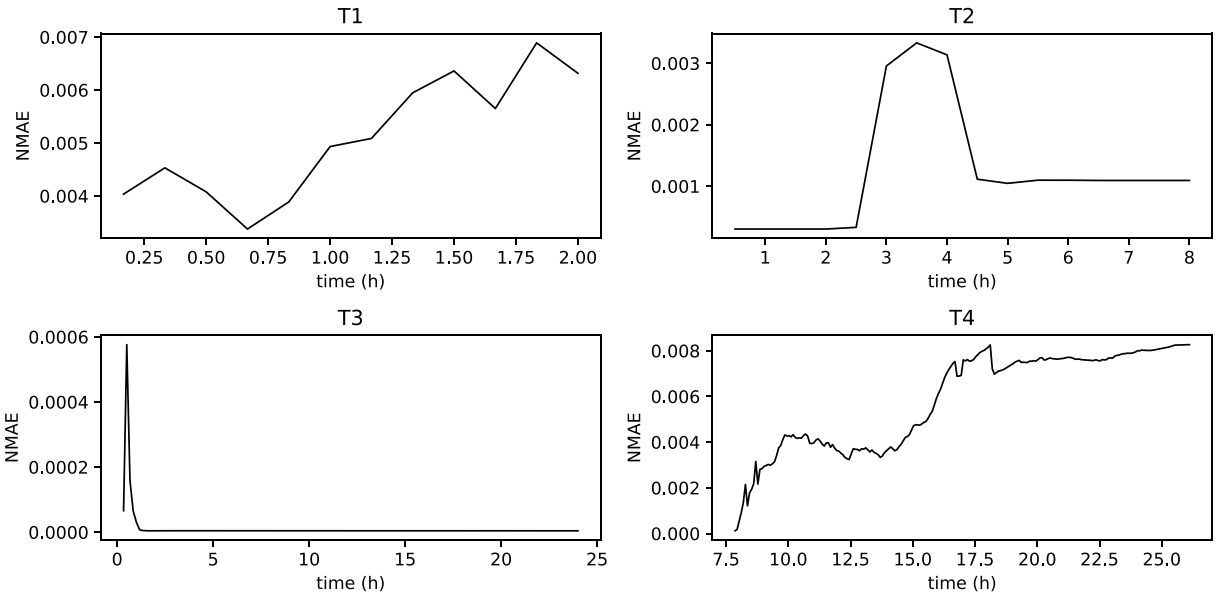

Fig. 11. Normalised mean absolute error evolution of the two proposed implementations for the four proposed test cases.

captured by the model with erosion depth reaching 2–4 m. Note that since the LiDAR data were taken while the water level was still relatively high in the Tinée River (see the flooded area represented as a hatched area in Fig. 9e), the reference erosion and deposition contour lines in Fig. 9g should not be analysed in this area, the *post*-event data being the free surface level and not the actual terrain level.

Further investigations must be performed to fully understand the dynamics of this case study, which includes massive deposition and erosion at fan and confluences between steep creeks and mountain valley rivers, during an extreme flood event. The results of this test case show that the soil erosion module presented here can be used for that purpose.

5. Computational efficiency

As described in Section 3.2 two implementations of the soil erosion model were developed. The main one was developed to run on CPUs in a single thread, meanwhile the GPU-enhanced implementation was developed to leverage the parallelism present in general purpose graphic cards. Both implementations were compared in terms of accuracy and computational efficiency using the four test cases proposed in the previous section. In test case T2, only the storm event R3 was chosen from the four events analysed, due its higher computational burden, while in test case T3 the spatially variable rainfall scenario was used.

In order to quantify the difference between the two solvers solutions, the normalised mean absolute error (NMAE) was calculated:

$$MAE = \frac{\sum_{i=1}^{N} |y_i - \hat{y}_i|}{N} \qquad NMAE = \frac{MAE}{|y_{max} - y_{min}|} \tag{19}$$

where N is the number of elements of the computational mesh, y_i are the values given by Iber, $\hat{y}_i$ are the values obtained from Iber+, y_{max} and y_{min} are the maximum a minimum values of the Iber simulation for a given time-step respectively. Fig. 11, shows the evolution of the NMAE for each of the proposed test simulations, keeping values below 0.0085 in all cases.

Several hardware configurations were used to compare both implementations (Table 6). The Iber package supports different hardware and software platforms. It can be run on Microsoft Windows and GNU/Linux operating systems, on systems ranging from servers to laptops using CPU and GPU computing. In the first configuration (CPU Server), the standard non-parallelised implementation of the model was run on a server with a CPU Intel Xeon Gold 6130. This will be considered as the baseline for performance comparison. Next, the GPU parallelised version was run on three different hardware configurations. First, a GPU computing server with a GPU Nvidia V100, a datacenter oriented graphics card released in 2017 with 5120 CUDA cores that offer nearly 15 TFLOPS (10^{12} floating-point operations per second) of theoretical peak throughput. Second, a standard desktop computer with a Nvidia RTX 3080 ti. This is a high-end consumer-grade graphics card released in 2021 with 10 240 CUDA cores that offers over 28 TFLOPS of computing power. Lastly, the model was also run in a laptop computer featuring an Nvidia RTX 3060, a mid-tier graphics card released in 2021 with 3584 CUDA cores and a reduced TDP (thermal design power) for mobile hardware. This limits its performance to nearly 11 TFLOPS. It should be considered that the performance of the GPUs mentioned above is based on peak values given by the manufacturer, and must be taken only as a rough indicator of their actual performance, which depends on many factors as the thermals, the configuration made by the assembler, or the software. The server configurations (CPU and GPU Server in Table 6) were run on the GRICAD (Grenoble Alpe Research - Scientific Computing and Data Infrastructure) facilities and run on Debian GNU/Linux version 11 OS. The desktop computer configuration was run on Archlinux OS meanwhile the laptop computer was run on Windows 11 OS.

Table 7 shows the run-time for the different test cases and hardware configurations. Three performance metrics are evaluated for each hardware configuration: (a) the time needed to complete the main loop of the simulation (this excludes the initialisation time of the simulation), (b) the speedup compared with the non-parallelised configuration and (c) the throughput of the model expressed in millions of mesh elements processed per second that is computed as follows:

$$Throughput = \frac{n_{cells} \cdot n_{steps}}{t_{simulation}} \cdot 10^{-6} \tag{20}$$

where n_{cells} is the number of cells of the computational mesh, n_{steps} is the number of computational steps needed to complete the simulation and $t_{simulation}$ is the run-time in seconds of the main loop of the simulation. The first test case (T1) is expected to be the worst scenario for the GPU parallelised implementation. This case uses a computational mesh of just 120 elements, meaning that the level of parallelism present in this problem is much lower than in the other test cases. Therefore, in this case the parallelised implementation is not capable of exploiting in an effective way the parallel computing resources available.

Table 6
Hardware configurations employed for the performance measurements.

Configuration	Solver	CPU	GPU		
			Model	Throughput	TDP
CPU server	Iber	Intel Xeon Gold 6130	–	–	–
GPU server	Iber+	Intel Xeon Gold 5218R	Nvidia V100	14.9 TFLOPS	300 W
Desktop computer	Iber+	AMD Ryzen 7 2700X	Nvidia RTX 3080 ti	28.6 TFLOPS	400 W
Laptop computer	Iber+	Intel Core i7-11375H	Nvidia RTX 3060	10.7 TFLOPS	115 W

Table 7
Performance measurements obtained for the different test cases and hardware configurations.

Test case	CPU server			GPU server			Desktop computer			Laptop computer		
	Time (s)	Speedup	MCells/s	Time (s)	Speedup	MCells/s	Time (s)	Speedup	MCells/s	Time (s)	Speedup	MCells/s
T1	35	1	0.18	29	1.21	0.22	24	1.46	0.27	92	0.38	0.07
T2	155	1	1.37	9	17.22	23.29	8	19.38	26.20	28	5.54	7.49
T3	34 271	1	0.56	283	121.1	67.24	195	175.75	97.58	542	63.23	35.10
T4	31 646	1	1.82	451	70.17	129.11	406	77.95	141.68	828	38.22	69.59

The GPUs used have thousands of parallel computing units (or CUDA cores), but each single core is less powerful than a single CPU core. This implies that processing 120 elements in parallel in a GPU will not saturate its computing capabilities, leaving many of the resources unused. Therefore, in this case, the high computational capacity of the GPU cannot overcome the overhead of using it (e.g. GPU memory transfers, expensive synchronisations, etc.). As shown in Table 7, the T1 case ran in 38 s on the CPU server. The runs on the GPU server and on the desktop computer were just marginally faster (29 and 24 s respectively), while running on the laptop was significantly slower (92 s).

The T2 test case has a larger computational mesh of 3300 elements, which is still lower than the number of cores of the GPUs. However, it is large enough to see some significant performance gains compared with the CPU solver. While the CPU version took 161 s to finish the simulation, the GPU server and the desktop computer were able to perform the simulation over 17 and 19 times faster respectively, while the laptop ran 5 times faster. The performance in terms of the number of processed cells per second increased in all configurations compared to T1. In the CPU version, this value is over 7 times higher. This is mainly due to the higher presence of dry elements (that are much faster to process) in test case T2. Also, this case uses just a single class of soil particles, meanwhile T1 uses seven different classes that must be processed independently. It is noteworthy that in the case of the GPU configurations the number of cells processed per second was increased over 100 times in comparison with T1, denoting that this case is more effective in exploiting the parallel computing resources available on the GPU.

The test case T3 has the largest computational mesh from all the proposed cases, with 94,119 elements. This number of elements is expected to be large enough to show the full potential of the GPU implementation. This case took more than ten hours to be processed by the CPU configuration. However, it took less than five minutes on the GPU server, achieving a speedup of 121. It was even faster on the desktop computer, with a speed-up of 176 relative to the CPU. The laptop configuration achieved a speed-up of 63, showing the capabilities of GPU computing even on modest devices. In terms of throughput, the number of cells processed per second was reduced in the CPU compared with T2, decreasing from 1.37 MCells/s to 0.56, mostly due to the increase of soil particle classes (from 1 to 4) and the lower presence of dry elements in T3. However, in the case of the GPU configurations, the number of cells processed per second increased significantly due to the larger size of the mesh. Hence, the higher number of elements enabled a better exploitation of the parallel resources.

The last test case (T4) has a computational mesh of 45,314 elements. This is less than T3, hence a lower speedup was expected due to the lower occupancy of the GPU. This case took almost 9 h to be completed on the CPU, meanwhile it was completed on the GPU server in less than 8 min, achieving a speedup of 70. The desktop computer was a bit faster with a speedup of nearly 78, while the laptop computer, despite its limitations, was able to finish the simulation in less than 14 min (38 times faster than CPU). Even though the laptop was slower than the other two GPU configurations, the performance achieved in such a small form factor is remarkable. In terms of throughput, the CPU configuration shows similar values to T2, because the presence of dry elements is similar in both tests, and both include a single class of soil particles, indicating a similar computing cost per cell on average. However, in the case of GPU the throughput was higher than in T2 (due to the larger mesh) and T3 (due to more dry elements and less soil particle classes).

6. Conclusions

An implementation of a new fully distributed multiclass soil erosion module in the software package Iber+ was presented, which solves the 2D shallow water equations. The model considers the transport of sediment particles of different sizes by overland flows, due to bed load and suspended load. The rainfall-driven and runoff-driven erosion processes are considered independently as the source terms for the suspended load transport equation, using for that purpose the physically-based formulations that have been proposed, validated and published in previous experimental studies. A mass conservation equation is solved for each sediment class in order to compute the evolution of the mass of sediment particles in the soil layer.

The article included four test cases to illustrate the capabilities of the presented tool and shows that the numerical model is able to achieve good accuracy with the appropriate parameterisation. Based on these results, it can be concluded that the model can be used to analyse phenomena related to soil erosion and sediment transport by overland flow at spatial scales ranging from laboratory experiments to meso-scale catchments, with spatial discretisations ranging from a few cm (at small spatial scales) to several m (at the catchment scale). At the laboratory scale, in test case T1, the model has shown adequate accuracy in reproducing the observed data, making it a potential tool for analysing sediment size-selectivity processes. In real world scenarios, at the hillslope scale, the test case T2 has also shown accurate results for different rainfall events, suggesting that it can also be used to analyse soil erosion phenomena at these scales. The test case T3 illustrates the applicability of the model to larger scales, here the GPU-enhanced implementation of the model is able to simulate in just a few minutes the erosion generated in a meso-scale catchment by rainfall events of several hours, using a numerical mesh of circa 10^5 mesh elements. The last proposed scenario (test case T4), analyses bed load transport and flow driven erosion processes at the river reach scale. Despite the complexity of the case (very intense transport, changes in

topography reaching 10 m), the model has shown results compatible with the observed data, making it a promising tool for further research.

In terms of computational performance, the throughput of the GPU implementation (number of mesh elements processed per second) is highly dependent on the number of sediment classes, the number of mesh elements and the relative extension of dry zones in the domain. The throughput decreases as the number of sediment classes increases because more equations need to be solved. The throughput increases with the number of mesh elements as the GPU parallelism is more efficiently exploited through HPC techniques. The extension of dry zones also impacts throughput, since the number of mathematical operations to be performed in dry elements is much lower than in wet elements. For these reasons it is not possible to provide an overall quantification of the throughput. For instance, in the desktop configuration used in this work (Nvidia RTX 3080 ti) the throughput varied from 0.27 MCells/s in test case T1 (with a very low number of mesh elements, seven size classes and no dry regions) to 141 MCells/s in test case T4 (with a large number of mesh elements, one single size class and several dry regions). On the CPU sequential implementation the throughput is significantly lower varying from 0.18 MCells/s in test case T1 to 1.8 MCells/s in test case T4. Thus, the speed-ups achieved with the GPU implementation can reach up to two orders of magnitude in problems with around 50 k–100 k mesh elements using a Nvidia RTX 3080 Ti in a standard desktop.

One of the main limitations of the model in its current implementation, and with the currently available hardware, is its application to large catchments (of the order of 100 km^2, or larger) due to the computational cost, input data requirements and calibration efforts involved. It should also be noted that even though fully distributed models provide more information than semi-distributed or lumped models, they also require a high amount of data to adequately calibrate the model and obtain accurate results. Therefore, they may not be the most appropriate tool in many circumstances. Users should be aware of the limitations of these kind of tools and perform the necessary verifications before drawing any conclusions.

Future work should focus on the application of the model to the analysis of different kinds of soil erosion processes. For that purpose, the model is freely available to the scientific community, and can be downloaded as part of the software package Iber from www.iberaula.com.

Software and data availability

The Iber+ software used to perform the computation showed in this paper, as well as the four test cases and the related data are all openly and permanently available at https://entrepot.recherche.data.gouv.fr/dataverse/soilsedimentmodellingdata.

CRediT authorship contribution statement

Luis Cea: Conceptualisation, Methodology, Software, Investigation, Writing – original draft, Writing – review & editing. **Orlando García-Feal:** Conceptualisation, Methodology, Software, Investigation, Writing – original draft, Writing – review & editing. **Guillaume Nord:** Conceptualisation, Methodology,Investigation, Writing – original draft, Writing – review & editing. **Guillaume Piton:** Conceptualisation, Methodology,Investigation, Writing – original draft, Writing – review & editing. **Cédric Legoût:** Conceptualisation, Methodology, Investigation, Writing – original draft, Writing – review & editing.

Declaration of competing interest

The authors declare that they have no known competing financial interests or personal relationships that could have appeared to influence the work reported in this paper.

Data availability

The software used to perform the computations and the data related to the test cases are openly available at https://entrepot.recherche.data.gouv.fr/dataverse/soilsedimentmodellingdata.

Acknowledgements

Funding for open access charge: Universidade da Coruña/CISUG. O.G.-F. was supported by the postdoctoral fellowship "Juan de la Cierva" (ref. JDC2022-048667-I), funded by MCIN/AEI/10.13039/501100011033 and the European Union "NextGenerationEU"/PRTR; by the Spanish Ministerio de Universidades under application 33.50.460A.752, by the European Union NextGenerationEU/PRTR through a contract Margarita Salas from the University of Vigo; by the IGE lab and by the French Ministry of Environment (Direction Générale de la Prévention des Risques Ministère de la Transition Ecologique et Solidaire) within the multirisk agreement SRNH-IRSTEA 2020 (Action TorRex). G.N. and C.L. were supported by the Labex OSUG@2020 (Investissements d'Avenir, grant agreement ANR-10-LABX-0056). G.P. was supported by the LabEx Tec21 (Investissements d'avenir - grant agreement n° ANR-11-LABX-0030). Some of the computations presented in this paper were performed using the GRICAD high performance infrastructure (https://gricad.univ-grenoble-alpes.fr), which is supported by the Rhône-Alpes region (GRANT CPER07_13 CIRA) and the Equip@Meso project (Investissements d'avenir - grant agreement n° ANR-10-EQPX-29-01).

References

Arnold, J., Allen, P., Volk, M., Williams, J., Bosch, D., 2010. Assessment of different representations of spatial variability on SWAT model performance. Trans. ASABE 53 (5), 1433–1443.

Arnold, J.G., Srinivasan, R., Muttiah, R.S., Williams, J.R., 1998. Large area hydrologic modeling and assessment part I: Model development 1. JAWRA J. Am. Water Resour. Assoc. 34 (1), 73–89.

Baldock, T.E., Tomkins, M.R., Nielsen, P., Hughes, M.G., 2004. Settling velocity of sediments at high concentrations. Coast. Eng. 51 (1), 91–100.

Batista, P.V., Davies, J., Silva, M.L., Quinton, J.N., 2019. On the evaluation of soil erosion models: Are we doing enough? Earth-Sci. Rev. 197, 102898.

Belikov, E., Deligiannis, P., Totoo, P., Aljabri, M., Loidl, H.-W., 2013. A Survey of High-Level Parallel Programming Models. Heriot-Watt University, Edinburgh, UK, p. 46, URL http://www.macs.hw.ac.uk/cs/techreps/docs/files/HW-MACS-TR-0103.pdf.

Beuselinck, L., Govers, G., Hairsine, P.B., Sander, G.C., Breynaert, M., 2002. The influence of rainfall on sediment transport by overland flow over areas of net deposition. J. Hydrol. 257, 145–163.

Beuselinck, L., Govers, G., Steegen, A., Hairsine, P.B., Poesen, J., 1999. Evaluation of the simple settling theory for predicting sediment deposition by overland flow. Earth Surf. Process. Landf. 24, 993–1007.

Beven, K., 2006. A manifesto for the equifinality thesis. J. Hydrol. 320 (1–2), 18–36.

Bladé, E., Cea, L., Corestein, G., Escolano, E., Puertas, J., Vázquez-Cendó, E., Dolz, J., Coll, A., 2014. Iber: herramienta de simulación numérica del flujo en ríos. Rev. Int. Metodos Numer. para Calc. Diseno Ing. 30 (1), 1–10.

Boudevillain, B., Delrieu, G., Galabertier, B., Bonnifait, L., Bouilloud, L., Kirstetter, P.E., Mosini, M.L., 2011. The cévennes-vivarais mediterranean hydrometeorological observatory database. Water Resour. Res. 47 (7).

Brigode, P., 2021. Première modélisation des débits générés par la tempête Alex (octobre 2020) dans les Alpes-Maritimes. Technical Report, Géoazur, UMR 7329, 250 rue Albert Einstein, Université Sophia Antipolis, Valbonne, France, URL https://hal.science/hal-03894853.

Brufau, P., García-Navarro, P., Vázquez-Cendón, M.E., 2004. Zero mass error using unsteady wetting-drying conditions shallow flows over dry of irregular topography. Internat. J. Numer. Methods Fluids 45, 1047–1082.

Buttinger-Kreuzhuber, A., Konev, A., Horváth, Z., Cornel, D., Schwerdorf, I., Blöschl, G., Waser, J., 2022. An integrated GPU-accelerated modeling framework for high-resolution simulations of rural and urban flash floods. Environ. Model. Softw. 156, 105480.

Carlotto, T., Chaffe, P.L.B., dos Santos, C.I., Lee, S., 2021. SW2D-GPU: A two-dimensional shallow water model accelerated by GPGPU. Environ. Model. Softw. 145, 105205.

Carlotto, T., da Silva, R.V., Grzybowski, J.M.V., 2019. GPGPU-accelerated environmental modelling based on the 2D advection-reaction-diffusion equation. Environ. Model. Softw. 116, 87–99.

Carrega, P., Michelot, N., 2021. Une catastrophe hors norme d'origine météorologique le 2 octobre 2020 dans les montagnes des Alpes-Maritimes. Physio-Géo (Volume 16), 1–70. http://dx.doi.org/10.4000/physio-geo.12370.

Cea, L., Alvarez, M., Puertas, J., 2022. Estimation of flood-exposed population in data-scarce regions combining satellite imagery and high resolution hydrological-hydraulic modelling: A case study in the licungo basin (mozambique). J. Hydrol.: Reg. Stud. 44, 101247.

Cea, L., Bladé, E., 2015. A simple and efficient unstructured finite volume scheme for solving the shallow water equations in overland flow applications. Water Resour. Res. 51 (7), 5464–5486.

Cea, L., Garrido, M., Puertas, J., 2010. Experimental validation of two-dimensional depth-averaged models for forecasting rainfall-runoff from precipitation data in urban areas. J. Hydrol. 382, 88–102.

Cea, L., Legout, C., Darboux, F., Esteves, M., Nord, G., 2014. Experimental validation of a 2D overland flow model using high resolution water depth and velocity data. J. Hydrol. 513, 142–153.

Cea, L., Legout, C., Grangeon, T., Nord, G., 2016. Impact of model simplifications on soil erosion predictions: Application of the GLUE methodology to a distributed event-based model at the hillslope scale. Hydrol. Process. 30 (7), 1096–1113.

Cea, L., Puertas, J., Vázquez-Cendón, M.E., 2007. Depth averaged modelling of turbulent shallow water flow with wet-dry fronts. Arch. Comput. Methods Eng. (ARCME) 14 (3).

Cea, L., Vázquez-Cendón, M.E., 2012. Unstructured finite volume discretisation of bed friction and convective flux in solute transport models linked to the shallow water equations. J. Comput. Phys. 231, 3317–3339.

Church, M., Jakob, M., 2020. What is a debris flood? Water Resour. Res. 56 (8), http://dx.doi.org/10.1029/2020WR027144.

Costabile, P., Costanzo, C., 2021. A 2D-SWEs framework for efficient catchment-scale simulations: Hydrodynamic scaling properties of river networks and implications for non-uniform grids generation. J. Hydrol. 599, 126306.

Coulthard, T.J., Skinner, C.J., 2016. The sensitivity of landscape evolution models to spatial and temporalrainfall resolution. Earth Surf. Dyn. 4 (3), 757–771. http://dx.doi.org/10.5194/esurf-4-757-2016, URL https://esurf.copernicus.org/articles/4/757/2016/.

Domínguez, J.M., Fourtakas, G., Altomare, C., Canelas, R.B., Tafuni, A., García-Feal, O., Martínez-Estévez, I., Mokos, A., Vacondio, R., Crespo, A.J.C., Rogers, B.D., Stansby, P.K., Gómez-Gesteira, M., 2021. DualSPHysics: from fluid dynamics to multiphysics problems. Comput. Part. Mech. http://dx.doi.org/10.1007/s40571-021-00404-2.

Esteves, M., Legout, C., Navratil, O., Evrard, O., 2019. Medium term high frequency observation of discharges and suspended sediment in a mediterranean mountainous catchment. J. Hydrol. 568, 562–574.

Ferraro, D., Costabile, P., Costanzo, C., Petaccia, G., Macchione, F., 2020. A spectral analysis approach for the a priori generation of computational grids in the 2-D hydrodynamic-based runoff simulations at a basin scale. J. Hydrol. 582, 124508.

Flanagan, D., Frankenberger, J., Ascough II, J., 2012. WEPP: Model use, calibration, and validation. Trans. ASABE 55 (4), 1463–1477.

Foster, G.R., Flanagan, D.C., Nearing, M.A., Lane, L.J., Risse, L.M., Finkner, S.C., 1995. In: Flanagan, D., Nearing, M. (Eds.), Water Erosion Prediction Project: Hillslope Profile and Watershed Model Documentation. USDA-ARS National Soil Erosion Research Laboratory, West Lafayette, Indiana.

Fu, B., Merritt, W.S., Croke, B.F., Weber, T.R., Jakeman, A.J., 2019. A review of catchment-scale water quality and erosion models and a synthesis of future prospects. Environ. Model. Softw. 114, 75–97.

Gao, B., Walter, M.T., Steenhuis, T.S., Parlange, J.Y., Nakano, K., Hogarth, W.L., Rose, C.W., 2003. Investigating ponding depth and soil detachability for a mechanistic erosion model using a simple experiment. J. Hydrol. 277 (1–2), 116–124.

Garcia, M.H., 2006. Sedimentation Engineering: Processes, Measurements, Modeling, and Practice. ASCE, Reston, Virginia.

García-Alén, G., González-Cao, J., Fernández-Nóvoa, D., Gómez-Gesteira, M., Cea, L., Puertas, J., 2022. Analysis of two sources of variability of basin outflow hydrographs computed with the 2D shallow water model Iber: Digital terrain model and unstructured mesh size. J. Hydrol. 612, 128182.

García-Feal, O., Cea, L., González-Cao, J., Manuel Domínguez, J., Gómez-Gesteira, M., 2020. IberWQ: A GPU accelerated tool for 2D water quality modeling in rivers and estuaries. Water 12, 413. http://dx.doi.org/10.3390/w12020413, URL https://www.mdpi.com/2073-4441/12/2/413.

García-Feal, O., González-Cao, J., Gómez-Gesteira, M., Cea, L., Domínguez, J.M., Formella, A., 2018. An accelerated tool for flood modelling based on Iber. Water 10 (10), 1459.

Garland, M., Grand, S.L., Nickolls, J., Anderson, J., Hardwick, J., Morton, S., Phillips, E., Zhang, Y., Volkov, V., 2008. Parallel computing experiences with CUDA. IEEE Micro 28, 13–27. http://dx.doi.org/10.1109/MM.2008.57.

Govers, G., 1992. In: Parsons, A., Abrahams, A. (Eds.), Overland flow, Hydraulics and Erosion Mechanics. University College London Press.

Grand, S.L., Götz, A.W., Walker, R.C., 2013. SPFP: Speed without compromise—A mixed precision model for GPU accelerated molecular dynamics simulations. Comput. Phys. Comm. 184, 374–380. http://dx.doi.org/10.1016/j.cpc.2012.09.022, URL https://linkinghub.elsevier.com/retrieve/pii/S0010465512003098.

Grangeon, T., 2012. Etude Multi-Échelle De La Granulométrie Des Particules Fines Générées Par Érosion Hydrique: Apports Pour La Modélisation (Ph.D. thesis). Université de Grenoble.

Hairsine, P.B., Rose, C.W., 1992a. Modeling water erosion due to overland-flow using physical principles. 1. Sheet flow. Water Resour. Res. 28 (1), 237–243.

Hairsine, P.B., Rose, C.W., 1992b. Modeling water erosion due to overland-flow using physical principles. 2. Rill flow. Water Resour. Res. 28 (1), 245–250.

Heng, B.C.P., Sander, G.C., Armstrong, A., Quinton, J.N., Chandler, J.H., Scott, C.F., 2011. Modeling the dynamics of soil erosion and size-selective sediment transport over nonuniform topography in flume-scale experiments. Water Resour. Res. 47 (2), W02513.

Hong, Y., Bonhomme, C., Le, M.H., Chebbo, G., 2016. A new approach of monitoring and physically-based modelling to investigate urban wash-off process on a road catchment near Paris. Water Res. 102, 96–108.

Jakob, M., Davidson, S., Bullard, G., Busslinger, M., Collier-Pandya, B., Grover, P., Lau, C.-A., 2022. Debris-flood hazard assessments in steep streams. Water Resour. Res. 58 (4), http://dx.doi.org/10.1029/2021WR030907.

Jomaa, S., Barry, D.A., Brovelli, A., Sander, G.C., Parlange, J.Y., Heng, B.C.P., van Meerveld, H.J.T., 2010. Effect of raindrop splash and transversal width on soil erosion: Laboratory flume experiments and analysis with the hairsine-rose model. J. Hydrol. 395, 117–132.

Kawanisi, K., Shiozaki, R., 2008. Turbulent effects on the settling velocity of suspended sediment. J. Hydraul. Eng. 134 (2), 261–266.

Kinnell, P.I.A., 1990. The mechanics of raindrop induced flow transport. Aust. J. Soil Res. 28, 497–516.

Kinnell, P.I.A., 2005. Raindrop-impact-induced erosion processes and prediction: A review. Hydrol. Process. 19, 2815–2844.

Le, P.V., Kumar, P., Valocchi, A.J., Dang, H.-V., 2015. GPU-based high-performance computing for integrated surface–sub-surface flow modeling. Environ. Model. Softw. 73, 1–13.

Legout, C., Freche, G., Biron, R., Esteves, M., Navratil, O., Nord, G., Uber, M., Grangeon, T., Hachgenei, N., Boudevillain, B., et al., 2021. A critical zone observatory dedicated to suspended sediment transport: The meso-scale galabre catchment (southern French Alps). Hydrol. Process. 35 (3), e14084.

Legout, C., Poulenard, J., Nemery, J., Navratil, O., Grangeon, T., Evrard, O., Esteves, M., 2013. Quantifying suspended sediment sources during runoff events in headwater catchments using spectrocolorimetry. J. Soils Sediments 13 (8), 1478–1492.

LeVeque, R.J., 2002. Finite Volume Methods for Hyperbolic Problems. Cambridge Texts in Applied Mathematics, vol. 31, Cambridge University Press.

Li, R.M., 1979. In: Shen, H.W. (Ed.), Modeling in Rivers. Wiley, New-York.

Liébault, F., Melun, G., Piton, G., Chapuis, M., Passy, P., Tacon, S., 2024. Channel change during catastrophic flood: Example of Storm Alex in the Vésubie and Roya valleys. Geomorphology 446, 109008. http://dx.doi.org/10.1016/j.geomorph.2023.109008.

Tromp-van Meerveld, H., Parlange, J.-Y., Barry, D.A., Tromp, M., Sander, G.C., Walter, M.T., Parlange, M.B., 2008. Influence of sediment settling velocity on mechanistic soil erosion modeling. Water Resour. Res. 44 (6), W06401. http://dx.doi.org/10.1029/2007WR006361.

Merrill, D., 2013. CUB: CUDA unbound. URL https://nvlabs.github.io/cub/.

Michalakes, J., Vachharajani, M., 2008. GPU acceleration of numerical weather prediction. Parallel Process. Lett. 18, 531–548. http://dx.doi.org/10.1142/S0129626408003557.

Morales-Hernández, M., Sharif, M.B., Kalyanapu, A., Ghafoor, S.K., Dullo, T.T., Gangrade, S., Kao, S.-C., Norman, M.R., Evans, K.J., 2021. TRITON: A multi-GPU open source 2D hydrodynamic flood model. Environ. Model. Softw. 141, 105034.

Morgan, R., Quinton, J., Smith, R., Govers, G., Poesen, J., Auerswald, K., Chisci, G., Torri, D., Styczen, M., 1998. The European soil erosion model (EUROSEM): A dynamic approach for predicting sediment transport from fields and small catchments. Earth Surf. Process. Landf.: J. Brit. Geomorphol. Group 23 (6), 527–544.

Mügler, C., Planchon, O., Patin, J., Weill, S., Silvera, N., Richard, P., Mouche, E., 2011. Comparison of roughness models to simulate overland flow and tracer transport experiments under simulated rainfall at plot scale. J. Hydrol. 402, 25–40.

Naves, J., Rieckermann, J., Cea, L., Puertas, J., Anta, J., 2020. Global and local sensitivity analysis to improve the understanding of physically-based urban wash-off models from high-resolution laboratory experiments. Sci. Total Environ. 709, 136152.

Nord, G., Boudevillain, B., Berne, A., Branger, F., Braud, I., Dramais, G., Gérard, S., Le Coz, J., Legout, C., Molinié, G., et al., 2017. A high space–time resolution dataset linking meteorological forcing and hydro-sedimentary response in a mesoscale mediterranean catchment (Auzon) of the Ardèche region, France. Earth Syst. Sci. Data 9 (1), 221–249.

Nord, G., Esteves, M., 2005. PSEM 2D: A physically based model of erosion processes at the plot scale. Water Resour. Res. 41 (W08407).

Nord, G., Esteves, M., 2007. Evaluation of sediment transport formulae and detachment parameters in eroding rills using PSEM2D and the water erosion prediction project (WEPP) database. Water Resour. Res. 43 (W08420), 1–14.

NVIDIA, 2023. CUDA C++ programming guide. URL https://docs.nvidia.com/cuda/pdf/CUDA_C_Programming_Guide.pdf.

Ouyang, C., Xiang, W., An, H., Wang, F., Yang, W., Fan, J., 2023. Mechanistic analysis and numerical simulation of the 2021 post-fire debris flow in xiangjiao catchment, China. J. Geophys. Res.: Earth Surf. 128 (1), e2022JF006846.

Pandey, A., Himanshu, S.K., Mishra, S.K., Singh, V.P., 2016. Physically based soil erosion and sediment yield models revisited. Catena 147, 595–620.

Pasquero, C., Provenzale, A., Spiegel, E.A., 2003. Suspension and fall of heavy particles in random two-dimensional flow. Phys. Rev. Lett. 91 (5), 054502.

Payrastre, O., Nicolle, P., Bonnifait, L., Brigode, P., Astagneau, P., Baise, A., Belleville, A., Bouamara, N., Bourgin, F., Breil, P., Brunet, P., Cerbelaud, A., Courapied, F., Devreux, L., Dreyfus, R., Gaume, E., Nomis, S., Poggio, J., Pons, F., Rabab, Y., Sevrez, D., 2022. Tempête Alex du 2 octobre 2020 dans les Alpes-Maritimes : Une contribution de la communauté scientifique à l'estimation des débits de pointe des crues. LHB 2082891. http://dx.doi.org/10.1080/27678490.2022.2082891.

Pignotti, G., Rathjens, H., Cibin, R., Chaubey, I., Crawford, M., 2017. Comparative analysis of HRU and grid-based SWAT models. Water 9 (4), http://dx.doi.org/10.3390/w9040272, URL https://www.mdpi.com/2073-4441/9/4/272.

Pimentel, D., Harvey, C., Resosudarmo, P., Sinclair, K., Kurz, D., McNair, M., Crist, S., Shpritz, L., Fitton, L., Saffouri, R., et al., 1995. Environmental and economic costs of soil erosion and conservation benefits. Science 267 (5201), 1117–1123.

Piton, G., Cohen, M., Flipo, M., Nowak, M., Chapuis, M., Melun, G., Robert, Y., Andréis, N., Liebault, F., 2024. Large in-stream wood yield during an extreme flood (Storm Alex, October 2020, Roya Valley, France): Estimating the supply, transport, and deposition using GIS. Geomorphology 446, 108981. http://dx.doi.org/10.1016/j.geomorph.2023.108981.

Piton, G., Recking, A., 2019. Steep bedload-laden flows: Near critical? J. Geophys. Res.: Earth Surf. 124 (8), 2160–2175. http://dx.doi.org/10.1029/2019JF005021.

Piton, G., Rodier, R., 2022. Comparaison Des Outils De Modélisation Des Évolutions Du Fond Par Charriage - Analyse Du Potentiel Et Des Limitations Des Outils De Modélisation 2D Sur Deux Cas D'étude. Technical Report, INRAE ETNA; DGPR (Direction Générale de la Prévention des Risques - Ministère de la Transition Ecologique et Solidaire), URL https://hal.inrae.fr/hal-03735959v1.

Poulenard, J., Legout, C., Nemery, J., Bramorski, J., Navratil, O., Douchin, A., Fanget, B., Perrette, Y., Evrard, O., Esteves, M., 2012. Tracing sediment sources during floods using diffuse reflectance infrared Fourier transform spectrometry (DRIFTS): A case study in a highly erosive mountainous catchment (southern French Alps). J. Hydrol. 414, 452–462.

van Rijn, L.C., 1984. Sediment transport, part II: Suspended load transport. J. Hydraul. Eng. 110 (11), 1613–1641.

Sanz-Ramos, M., Bladé, E., González-Escalona, F., Olivares, G., Aragón-Hernández, J.L., 2021. Interpreting the manning roughness coefficient in overland flow simulations with coupled hydrological-hydraulic distributed models. Water 13 (23), 3433.

Sanz-Ramos, M., López-Gómez, D., Bladé, E., Dehghan-Souraki, D., 2023. A CUDA fortran GPU-parallelised hydrodynamic tool for high-resolution and long-term eco-hydraulic modelling. Environ. Model. Softw. 161, 105628.

Sharma, P.P., Gupta, S.C., Foster, G.R., 1993. Predicting soil detachment by raindrops. Soil Sci. Am. J. 57, 674–680.

Sharma, P.P., Gupta, S.C., Foster, G.R., 1995. Raindrop-induced soil detachment and sediment transport from interrill areas. Soil Sci. Am. J. 59, 727–734.

Shaw, S.B., Parlange, J.Y., Lebowitz, M., Walter, M.T., 2009. Accounting for surface roughness in a physically-based urban wash-off model. J. Hydrol. 367, 79–85.

Shaw, S.B., Walter, M.T., Steenhuis, T.S., 2006. A physical model of particulate wash-off from rough impervious surfaces. J. Hydrol. 327, 618–626.

Shimizu, Y., Nelson, J., Arnez Ferrel, K., Asahi, K., Giri, S., Inoue, T., Iwasaki, T., Jang, C.-L., Kang, T., Kimura, I., et al., 2020. Advances in computational morphodynamics using the international river interface cooperative (iRIC) software. Earth Surf. Process. Landf. 45 (1), 11–37. http://dx.doi.org/10.1002/esp.4653.

Sun, Y., Bohm Agostini, N., Dong, S., Kaeli, D., 2019. Summarizing CPU and GPU design trends with product data. arXiv preprint arXiv:1911.11313 URL http://arxiv.org/abs/1911.11313.

Sutter, H., 2005. The free lunch is over: A fundamental turn toward concurrency in software. Dr. Dobb's J. 30, 1–9, URL http://www.mscs.mu.edu/~rge/cosc2200/homework-fall2013/Readings/FreeLunchIsOver.pdf.

Sutter, H., Larus, J., 2005. Software and the concurrency revolution. Queue 3, 54–62. http://dx.doi.org/10.1145/1095408.1095421.

Taccone, F., Antoine, G., Delestre, O., Goutal, N., 2018. A gravity-driven runoff and erosion model for sediment transfers at the catchment scale. In: Paquier, A., Rivière, N. (Eds.), E3S Web of Conferences. Vol. 40, p. 04019. http://dx.doi.org/10.1051/e3sconf/20184004019, URL https://www.e3s-conferences.org/10.1051/e3sconf/20184004019.

Tassi, P., Benson, T., Delinares, M., Fontaine, J., Huybrechts, N., Kopmann, R., Pavan, S., Pham, C.-T., Taccone, F., Walther, R., 2023. GAIA - A unified framework for sediment transport and bed evolution in rivers, coastal seas and transitional waters in the TELEMAC-MASCARET modelling system. Environ. Model. Softw. 159, 105544. http://dx.doi.org/10.1016/j.envsoft.2022.105544, URL https://linkinghub.elsevier.com/retrieve/pii/S1364815222002444.

Tatard, L., Planchon, O., Wainwright, J., Nord, G., Favis-Mortlock, D., Silvera, N., Ribolzi, O., Esteves, M., Huang, C.H., 2008. Measurement and modelling of high-resolution flow-velocity data under simulated rainfall on a low-slope sandy soil. J. Hydrol. 348 (1–2), 1–12.

Toro, E.F., 2001. Shock-capturing Methods for Free-Surface Shallow Flows. Wiley, Chichester, West Sussex PO19 1UD, England.

Toro, E.F., 2009. Riemann Solvers and Numerical Methods for Fluid Dynamics: A Practical Introduction. Springer-Verlag, New York.

Uber, M., Nord, G., Legout, C., Cea, L., 2021. How do modeling choices and erosion zone locations impact the representation of connectivity and the dynamics of suspended sediments in a multi-source soil erosion model? Earth Surf. Dyn. 9 (1), 123–144.

Vacondio, R., Dal Palù, A., Ferrari, A., Mignosa, P., Aureli, F., Dazzi, S., 2017. A non-uniform efficient grid type for GPU-parallel shallow water equations models. Environ. Model. Softw. 88, 119–137.

Vanzo, D., Peter, S., Vonwiller, L., Bürgler, M., Weberndorfer, M., Siviglia, A., Conde, D., Vetsch, D.F., 2021. BASEMENT v3: A modular freeware for river process modelling over multiple computational backends. Environ. Model. Softw. 143, 105102. http://dx.doi.org/10.1016/j.envsoft.2021.105102.

Vrugt, J.A., Ter Braak, C.J.F., Hoshin, G.V., Robinson, B.A., 2009. Equifinality of formal (DREAM) and informal (GLUE) Bayesian approaches in hydrologic modeling? Stoch. Environ. Res. Risk Assess. 23 (7), 1011–1026.

Williams, J.R., Jones, C.A., Dyke, P.T., 1984. A modeling approach to determining the relationship between erosion and soil productivity. Trans. ASAE 27 (1), 129–0144.

Xilin, X., Qiuhua, L., Xiaodong, M., 2019. A full-scale fluvial flood modelling framework based on a high-performance integrated hydrodynamic modelling system (HiPIMS). Adv. Water Resour. 132, 103392.

Yin, D., Xue, Z.G., Gochis, D.J., Yu, W., Morales, M., Rafieeinasab, A., 2020. A process-based, fully distributed soil erosion and sediment transport model for WRF-hydro. Water 12 (6), 1840.